PHYSICAL REVIEW D **110,** 014028 (2024)

Impact of nonzero strangeness and momentum anisotropy on thermodynamics of finite volume quark matter

Nisha Chahal,[*] Suneel Dutt,[†] and Arvind Kumar[‡]
Department of Physics, Dr. B R Ambedkar National Institute of Technology,
Jalandhar-144008, Punjab, India

(Received 7 March 2024; accepted 11 June 2024; published 19 July 2024)

This paper investigates the impact of strangeness chemical potential and anisotropic momentum distribution on finite-size isospin asymmetric quark matter by employing a three-flavored Polyakov quark meson model. The model incorporates scalar and vector interactions to investigate the critical endpoint (CEP) and the susceptibilities of conserved charges in isotropic and anisotropic medium. The chiral critical point in the QCD phase diagram is found to be shifted toward higher values of the quark chemical potential (μ_q) and lower temperature (T) for decreasing system size. On the other hand, there is an opposite change to lower quark chemical potential and higher temperature for decreasing strangeness chemical potential. The impact of anisotropic momentum distribution is discussed in terms of anisotropy parameter, ξ. It is found that as the value of ξ increases toward a positive value, the chiral phase boundary becomes a crossover. The Polyakov loop potential is introduced in the model to analyze the change in the deconfinement transition line.

DOI: 10.1103/PhysRevD.110.014028

I. INTRODUCTION

Thermodynamics of strongly interacting matter, such as quark-gluon plasma (QGP), is of tremendous interest to theoretical and experimental physicists [1,2]. Heavy ion collision (HIC) experiments like the Large Hadron Collider (LHC) [3] at CERN in Switzerland and the Relativistic Heavy Ion Collider (RHIC) at Brookhaven National Laboratory [4,5] are crucial in recreating the conditions of the early universe to understand the properties of QGP better. In addition to the experimental facilities, lattice quantum chromodynamics (QCD) simulations are also a powerful technique for calculating the QCD partition function on a discrete space-time lattice [6]. It is a nonperturbative application of field theory based on the Feynman path integral technique and can also be used to study some important hadron properties [7–9]. The hadronic tensor has been computed on the lattice to encompass the inclusive contribution of all intermediate states, which is crucial for understanding neutrino scattering experiments at low energies [10]. Also, a novel perspective on hadronic parity violation by considering four quark operators has been highlighted in lattice studies [11]. The pressure, energy density, and susceptibilities of conserved charges can be obtained using lattice QCD simulations of thermodynamic phenomena. At high temperatures and low baryonic densities, these computations have anticipated a crossover transition from the confined to the deconfined state [12]. On the other hand, due to the sign problem at higher baryonic chemical potentials and low-temperature values, the phase fluctuations derived from the complex fermion determinant are found to be very large [13].

In HICs, after the formation of QGP, it expands rapidly and cools down to form hadrons in a small region of space. Due to the finite size of colliding nuclei and the geometry of the collision, the fireball created in the initial stage is a finite-sized system. In this case, the finite size refers to the influence of the QGP's finite volume on its properties and evolution. Finite-size effects can affect particle flow, hadronization, and other variables sensitive to QGP properties [14,15]. In conjunction with experimental and simulation facilities, QCD low-energy effective models contribute to a nuanced and comprehensive exploration of the complexities inherent in studying QCD matter [16–23]. The quark-meson model has been earlier utilized to assess the impact of finite volume and long-range fluctuations [24,25]. The effect of finite volume on the QCD phase diagram has also been analyzed considering different boundary conditions, such as stationary, periodic, and antiperiodic for cubic and spherical regions [15]. On the basis of the pion mass, it has been observed that the curvature, which is defined as the second derivative of the chiral condensate with respect to temperature and chemical potential, continually decreases for periodic and antiperiodic boundary conditions as a function of system size, thus indicating that the phase transition boundary may shift in a

---

[*] Contact author: nishachahal137@gmail.com
[†] Contact author: dutts@nitj.ac.in
[‡] Contact author: kumara@nitj.ac.in

finite volume [14]. For low chemical potential values, the impact of finite size effects on the curvature of the chiral transition boundary has also been studied in lattice QCD [26,27]. By using a lower momentum cutoff in the Polyakov Nambu-Jona-Lasinio (PNJL) model, transport properties are observed to be enhanced in lower temperature regimes, whereas they become independent for higher values of temperatures [28]. The finite size effects have been utilized in the literature to explore the impact of the magnetic field, study the phase structure of difermion, and investigate the thermodynamic properties of QCD matter [29–34]. In investigating finite volume quark matter in the PQM model, the phase transition lines tend to crossover with decreasing system volume, and the phase transition line shifts to the higher value of quark chemical potential and temperature [22,23]. On the contrary, the phase transition line is found to shift to low quark chemical potential and temperature for decreasing system volume in the PNJL model [35–37]. However, the CEP is shifted to a higher quark chemical potential and lower temperature in both PQM and PNJL approaches. An opposite change in CEP to higher quark chemical potential and temperature is observed for the Polyakov chiral quark mean field model [34]. Thus, studying finite volume effects on the QCD phase diagram requires further investigation to understand the phase transitions and CEP behavior, modeling physical systems, and developing effective theoretical frameworks.

In order to study the phase transitions in the QCD phase diagram, an isotropic momentum distribution is usually taken into account in the theoretical models and lattice QCD studies. A departure from perfect isotropy is being anticipated in a real quark-gluon plasma. Hence, it becomes essential to study the various properties of anisotropic quark matter, which is characterized by varying expansion rates along the longitudinal and radial directions of the fireball produced in HICs. This involves manipulating the isotropic distribution by stretching or squeezing it in a specific direction [38]. The nonequilibrium state of QGP governed by instability with respect to color collective modes can significantly impact the dynamical evolution of a QGP [39]. These unstable modes can potentially expedite the processes of thermalization and isotropization, particularly of the softer modes within the QGP [40]. In essence, these modes, marked by their exponential amplification, contribute to a more rapid redistribution of energy and momentum, facilitating the establishment of local thermal equilibrium [41]. This conceptual framework enables the incorporation of anisotropy in the momentum distribution of particles, providing a practical means to describe the asymmetrical nature of their motion within the given system [42]. In prior investigations, ellipsoidal momentum anisotropy, which considers two independent anisotropy parameters, has been employed to calculate the dispersion relations and self-energies of the quark-gluon plasma at high temperatures [40,43]. It has been suggested that the production of high-energy photons is influenced by the assumed degree of initial momentum-space anisotropy in the quark-gluon plasma. Therefore, it might be feasible to experimentally determine the early-time momentum-space anisotropy of the quark-gluon plasma produced in relativistic heavy-ion collisions by examining high-energy photon yields [44–46]. In the framework of the relaxation time approximation and solving the Boltzmann kinetic equation, the transport coefficients for the quark-gluon plasma phase have been calculated by considering momentum anisotropy originating from varying expansion rates along the longitudinal and transverse directions of the medium [47,48]. The chiral phase structure of quark matter within the $(2+1)$ flavor quark-meson model (in the absence of Polyakov loop and vector interactions), characterized by spheroidal momentum-space anisotropy determined by a single anisotropy parameter, ξ, has been studied earlier [49]. Also, the variation of the average momentum and the distribution function of quarks with respect to angular orientation has been studied in the framework of the PNJL model. Thus, the study of anisotropic quark matter becomes an essential parameter while analyzing the QCD critical endpoint.

Along with the investigation of finite volume anisotropic quark matter, the concept of finite strangeness chemical potential is critical to our understanding of the fundamental building blocks of the universe. By fitting observed particle ratios, studies have estimated μ_S to be approximately 2% to 30% of the baryonic chemical potential [50–52]. These findings underscore the significance of nonzero strangeness chemical potential despite its modest but significant value. Incorporating finite strangeness chemical potential into the study of quark matter allows us to investigate the behavior of strange quarks in this exotic condition. Strangeness enhancement in heavy-ion collisions serves as a signature of the deconfinement phase transition, provides insights into thermalization and strangeness equilibration, influences the equation of state of nuclear matter and the QGP, and helps in understanding the dynamics of hadronization [53–56]. The large value of strangeness has been shown to affect the generation of neutron twin stars, which can predict the existence of first-order phase transition at lower temperatures and higher density values [57]. In the framework of the Hadron resonance gas (HRG) model, it has been highlighted that the critical temperature decreases with the increase in the value of strangeness chemical potential [58]. Therefore, the quark-hadron phase boundary is modified as a consequence of finite strangeness chemical potential considerations [59].

In the investigation of QCD matter, the susceptibilities of conserved charges are particularly significant observables [60–62]. These have been recognized as observables that can be theoretically and experimentally estimated better to understand the CEP. It has been demonstrated in recent studies that fluctuations in net-kaon and net-pion fluctuations are predominantly influenced by resonance contributions, unlike protons, thereby rendering them effective indicators of baryon number fluctuations [63]. In the HRG model, it has been concluded that differences and ratios of susceptibilities offer crucial insights into interactions, furnishing significant details about deviations from an ideal gas model [64]. Studying the susceptibilities of conserved charges in finite volumes has gained popularity recently since it can shed light on the nature of QCD phase transitions and the equation of state of QCD matter in practical experimental settings [33,65]. In the PQM model, the interaction of quarks is governed by the exchange of scalar and vector mesons, each playing a distinct role in the dynamics of hadronic matter. Scalar mesons induce an attractive force between quarks, essential for binding them together to form mesons and baryons, whereas vector mesons introduce a repulsive force between quarks. This repulsion arises from the exchange of vector mesons, which mediate the interaction between quarks, preventing the collapse of hadrons under the strong interaction. At low temperatures and densities, the dominant attractive scalar interactions lead to the formation of bound quark states, while at higher temperatures or densities, the repulsive vector interactions become more prominent, influencing the thermodynamic properties of the system [66–68]. The introduction of vector interactions has been found to impact the position of the QCD endpoint in the mean field as well as in the functional renormalization group (FRG) approach [69,70]. In FRG, enhancing the repulsive vector interaction has shifted the CEP toward high temperature and lower chemical potential values in the two-flavor quark meson model [69] whereas, in the three-flavor PQM model with vector interaction, the CEP has been found to shift to lower value of temperature and higher quark chemical potential [67,70,71]. Hence, in order to study the thermodynamic characteristics of finite volume isospin asymmetric strange quark matter in anisotropic momentum space, it is essential to include vector meson interactions to attain a comprehensive understanding of the phase diagram. In the present work, we use the three-flavored Polyakov quark-meson model, extended by the inclusion of vector interactions and isospin asymmetry, to study the thermodynamics of finite volume quark matter for the nonzero value of strangeness chemical potential and anisotropic distribution of momentum.

This paper is organized as follows: In Sec. II, we present the details of the PQM model and the introduction of momentum space anisotropy in the finite volume quark matter. In Sec. III, the impact of the nonzero value of strangeness chemical potential and anisotropic momentum parameter in finite volume quark matter on various thermodynamic variables and the QCD phase diagram have been discussed. In Sec. IV, the critical findings of the current work have been summarized.

II. POLYAKOV QUARK MESON MODEL

The chiral quark meson model is an effective approach to study the strong interactions between mesons and quarks. The spontaneous breaking of the chiral symmetry in a vacuum is described by including a scalar field that represents the chiral condensate. It is a nonperturbative model based on the mean-field approximation to study the thermodynamic properties of the system. The model has been used to study various phenomena in QCD, such as the properties of hadrons, the phase structure of QCD at finite temperature and density, and the properties of quark-gluon plasma created in heavy-ion collisions [72,73]. It has also been used to study the behavior of matter under extreme conditions, such as the properties of neutron stars and the early universe [67,74]. The total Lagrangian of the model for N_f flavors is given by [66,75]

$$\begin{aligned}\mathcal{L} = {}& \bar{\Psi} i\gamma^{\mu}\partial_{\mu}\Psi + \mathrm{Tr}(\partial_{\mu}\varphi^{\dagger}\partial^{\mu}\varphi) - m^{2}\mathrm{Tr}(\varphi^{\dagger}\varphi) - \lambda_1[\mathrm{Tr}(\varphi^{\dagger}\varphi)]^{2} \\ & - \lambda_2[\mathrm{Tr}(\varphi^{\dagger}\varphi)^{2}] + c(\det(\varphi) + \det(\varphi^{\dagger})) + \mathrm{Tr}[H(\varphi + \varphi^{\dagger})] \\ & + \mathcal{L}_{qm} - \frac{1}{4}\mathrm{Tr}(V_{\mu\nu}V^{\mu\nu}) + \frac{m_1^{2}}{2}V_{a\mu}V_{\mu}^{a}. \end{aligned} \tag{1}$$

In the above equation, $\Psi = (u, d, s)$ is the quark spinor for $N_c = 3$, color degrees of freedom and $\varphi = T_a(\sigma_a + i\gamma_5\pi_a)$, where $T_a = \lambda_a/2$ are Gell-Mann matrices. The first term in Eq. (1) accounts for the kinetic energy of massless quarks. The next two terms describe scalar mesons kinetic energy and mass term contributions. The terms involving λ_1 and λ_2 are quartic interaction terms, followed by the determinant term, which corresponds to $\mathrm{U}(1)_A$ anomaly in QCD vacuum [76] and explicit symmetry-breaking terms defined by $H = T_a h_a$. Through these symmetry-breaking terms, the σ meson has a finite vacuum expectation value (VEV) and, consequently, a finite quark mass [66]. The last two terms in the Lagrangian are incorporated to define the interaction with vector mesons. Here, vector mesons field tensor is represented as $V^{\mu\nu} = \partial^{\nu}V^{\mu} - \partial^{\mu}V^{\nu}$, where V^{μ} is multiplet of vector mesons. The second last term represents the kinetic energy, while the subsequent term denotes the mass term of vector mesons [66,77]. Due to $SU(3)_L \times SU(3)_R$ symmetry in the effective Lagrangian, the term representing the quark-meson interaction can be written as [75]

$$\begin{aligned}\mathcal{L}_{qm} = {}& g_s(\bar{\Psi}_L\varphi\Psi_R + \bar{\Psi}_R\varphi^{\dagger}\Psi_L) \\ & - g_v(\bar{\Psi}_L\gamma^{\mu}L_{\mu}\Psi_L + \bar{\Psi}_R\gamma^{\mu}R_{\mu}\Psi_R). \end{aligned} \tag{2}$$

Here, g_v and g_s represent the coupling constants for the vector and scalar mesons, respectively. In the above equation, L_{μ} and R_{μ} are defined in terms of pseudovector (A_{μ}^{a}) and vector (V_{μ}^{a}) mesons as

$$L_\mu(R_\mu) = \frac{1}{\sqrt{2}}\begin{pmatrix} \frac{\omega+\rho^0}{\sqrt{2}} & \rho^+ & K^{\star +} \\ \rho^- & \frac{\omega-\rho^0}{\sqrt{2}} & K^{\star 0} \\ K^{\star -} & K^{\star 0} & \phi \end{pmatrix}^\mu \pm \frac{1}{\sqrt{2}}\begin{pmatrix} \frac{f_1+a_1^0}{\sqrt{2}} & a_1^+ & K_1^+ \\ a_1^- & \frac{f_1-a_1^0}{\sqrt{2}} & K_1^0 \\ K_1^- & \bar{K}_1^0 & f_{1\phi} \end{pmatrix}^\mu . \tag{3}$$

To study the properties of chiral symmetry breaking and deconfinement within the PQM framework, the model is extended by introducing gauge-invariant Polyakov loop potential. The parameters of the Polyakov-loop potential are fitted to lattice data from the pure Yang-Mills system to incorporate the essential features of confinement and deconfinement transitions from purely gluonic interactions. The Polyakov loop serves as a well-defined order parameter in the limit of infinitely heavy quarks, where the dynamics of quarks become negligible, and gluonic interactions primarily govern the system's behavior [78,79]. Thus, the Polyakov loop effectively characterizes the transition from a confined phase, where color charges are confined within hadrons, to a deconfined phase, where they are free to move independently. In the infinite mass limit of quarks, the order parameter that contributes to confinement is determined by its expectation value. The Polaykov loop is defined in a manner that obeys the center symmetry [80] and is operationally defined as a Wilson loop in the temporal direction. This definition is expressed through the following formulation:

$$\wp(\vec{x}) = \mathcal{P}\exp\left[i\int_0^\beta d\tau \mathcal{A}_0(\vec{x},\tau)\right]. \tag{4}$$

Here, $\wp$ signifies the path-ordering, and $\mathcal{A}_0(\vec{x},\tau)$ denotes the Euclidean gauge field's temporal component [80,81]. The absence of a unique choice for the Polyakov loop potential in QCD stems from the intricate, nonperturbative nature of strong interactions, the interplay of confinement and chiral symmetry breaking, temperature and density dependencies, and diverse modeling approaches. In the current work, we use the polynomial form of the Polyakov loop defined as [82]

$$\frac{\mathcal{U}_{\mathrm{poly}}(\Phi,\bar{\Phi})}{T^4} = -\frac{b_2(T)}{2}\bar{\Phi}\Phi - \frac{b_3}{6}(\Phi^3+\bar{\Phi}^3) + \frac{b_4}{4}(\bar{\Phi}\Phi)^2, \tag{5}$$

and the temperature-dependent coefficient b_2 defined as

$$b_2(T) = a_0 + a_1\left(\frac{T_0}{T}\right) + a_2\left(\frac{T_0}{T}\right)^2 + a_3\left(\frac{T_0}{T}\right)^3. \tag{6}$$

As mentioned before, the parameters are determined by fitting the data to lattice simulations, which gives: $a_0 = 1.53$, $a_1 = 0.96$, $a_2 = -2.3$, $a_3 = -2.85$, $b_3 = 13.34$ and $b_4 = 14.88$ [83]. Using the total effective Lagrangian of the model, we obtain the thermodynamic potential given as

$$\begin{aligned}\Omega(\sigma_u,\sigma_d,\sigma_s,\omega,\rho,\phi,\Phi,\bar{\Phi};T,\mu_f) &= U(\sigma_u,\sigma_d,\sigma_s) + \Omega_{q\bar{q}}^{\mathrm{vac}}(\sigma_u,\sigma_d,\sigma_s) \\ &\quad + \mathcal{U}(\Phi,\bar{\Phi}:T,\mu_f) + \Omega_{q\bar{q}}^{th}(\sigma_u,\sigma_d,\sigma_s,\Phi,\bar{\Phi}:T,\mu_f) + V(\omega,\rho,\phi) - U_0(\sigma_{u0},\sigma_{d0},\sigma_{s0})\end{aligned} \tag{7}$$

where the mesonic potential, including the chiral symmetry-breaking terms, is described as [84]

$$\begin{aligned}U(\sigma_u,\sigma_d,\sigma_s) &= \frac{\lambda_1}{4}\left[\left(\frac{\sigma_u^2+\sigma_d^2}{2}\right)^2 + \sigma_s^4 + (\sigma_u^2+\sigma_d^2)\sigma_s^2\right] + \frac{\lambda_2}{4}\left(\frac{\sigma_u^4+\sigma_d^4}{4}+\sigma_s^4\right) \\ &\quad - \frac{c}{2\sqrt{2}}\sigma_u\sigma_d\sigma_s + \frac{m^2}{2}\left(\frac{\sigma_u^2+\sigma_d^2}{2}+\sigma_s^2\right) - \frac{h_{ud}}{2}(\sigma_u+\sigma_d) - h_s\sigma_s.\end{aligned} \tag{8}$$

Since vector-like gauge symmetries are not spontaneously broken in a vacuum, h_{ud} in the above equation represents the explicit symmetry breaking for the u and d quarks [85]. In the above equation, m^2 represents the tree-level mass of the fields in the absence of symmetry breaking, λ_1, λ_2 denote the two possible quartic coupling constants, and c stands for the cubic coupling constant. The parameters λ_1, λ_2, m^2, c, h_{ud} and h_s are determined by fitting the known decay constants f_π and f_K along with the masses of mesons such as m_π, m_K, m_σ and squared masses of η' and η mesons [86].

At vanishing temperature and baryonic chemical potential values, the dynamical chiral symmetry breaking is taken into account by the fermion vacuum term in the model represented by $\Omega_{q\bar{q}}^{\mathrm{vac}}(\sigma_u,\sigma_d,\sigma_s)$ in Eq. (7). Due to this term, the critical point is relocated to a lower temperature and higher baryonic chemical potential values [87,88]. Additionally, the vacuum potential energy, $U_0(\sigma_{u0},\sigma_{d0},\sigma_{s0})$ is subtracted to obtain the vanishing vacuum energy. The quark-antiquark interaction term is written as a combination of the vacuum mesonic fluctuations and thermal terms, $\Omega^{th}_{q\bar{q}}$, which is deduced from the fermionic determinant. These terms can be described as [88]

$$\Omega_{q\bar{q}} = \Omega^{\mathrm{vac}}_{q\bar{q}} + \Omega^{th}_{q\bar{q}} \tag{9}$$

where,

$$\Omega^{\mathrm{vac}}_{q\bar{q}} = -2N_c \sum_{f=u,d,s} \int \frac{d^3p}{(2\pi)^3} E^*_f = -\frac{N_c}{8\pi^2} \sum_{f=u,d,s} m_f^{*^4} \log\left[\frac{m^*_f}{\Lambda}\right], \tag{10}$$

$$\Omega^{th}_{q\bar{q}} = -2T \sum_{f=u,d,s} \int \frac{d^3p}{(2\pi)^3} [\ln g^+_f + \ln g^-_f]. \tag{11}$$

In above equation, g^+_f and g^-_f are defined as

$$g^+_f = [1 + 3\Phi e^{-(E^*_f - \mu^*_f)/T} + 3\bar{\Phi} e^{-2(E^*_f - \mu^*_f)/T} + e^{-3(E^*_f - \mu^*_f)/T}], \tag{12}$$

and

$$g^-_f = \left[1 + 3\bar{\Phi} e^{-(E^*_f + \mu^*_f)/T} + 3\Phi e^{-2(E^*_f + \mu^*_f)/T} + e^{-3(E^*_f + \mu^*_f)/T}\right]. \tag{13}$$

In Eq. (10), Λ is the regularization scale parameter. The effective single particle energy of the quarks is modified due to the interactions with mesons and is defined as $E^*_f = \sqrt{p^2 + m^{*2}_f}$. The m^*_f represents the effective mass of constituent quarks given by

$$m^*_u = \frac{g_s}{2}\sigma_u, \qquad m^*_d = \frac{g_s}{2}\sigma_d \quad \text{and} \quad m^*_s = \frac{g_s}{\sqrt{2}}\sigma_s. \tag{14}$$

The Yukawa coupling constant g_s value is determined by fixing the constituent quark mass for light quarks at $m_l = 300$ MeV. It has been studied in the quark meson model [67] that due to increased scalar coupling by increasing the constituent quark mass greater than or equal to 300 MeV, a first-order phase transition emerges, characterized by a sudden jump in the chiral condensate. A crossover transition has been observed for m_q values approximately less than or equal to 300 MeV. As m_q values increase further, the intensity of the first-order chiral phase transition also amplifies. In case of very low quark mass values, the scalar condensates would exhibit a smooth crossover-like behavior as a function of the chemical potential. In Eq. (7), the interaction term incorporating the nonstrange vector (ω) and vector-isovector field (ρ), along with strange vector field (ϕ) is written as $V(\omega,\rho,\phi) = -\frac{1}{2}(m^2_\omega \omega^2 + m^2_\rho \rho^2 + m^2_\phi \phi^2)$. The effective chemical potential of the quarks is modified as a consequence of vector-meson interactions [89] and is defined in terms of baryonic chemical potential, μ_B, isospin chemical potential, μ_I and strangeness chemical potential, μ_S as

$$\begin{aligned} \mu^*_u &= \mu_B/3 + \mu_I - g_{\omega u}\omega - g_{\rho u}\rho \\ \mu^*_d &= \mu_B/3 - \mu_I - g_{\omega d}\omega + g_{\rho d}\rho \\ \mu^*_s &= \mu_B/3 - \mu_S - g_{\phi s}\phi. \end{aligned} \tag{15}$$

In the above equation, the baryonic chemical potential is related to quark chemical potential as $\mu_B = 3\mu_q$. In the context of anisotropic quark matter, the modification of quasiparticle dispersion relations aligns with the anisotropic momentum distribution. In this case, the nontrivial dispersion relation for effective mass m^*_f is characterized by [40]

$$E^{*(\mathrm{aniso})}_f = \sqrt{p^2 + \xi(p.\hat{n})^2 + m^{*2}_f}. \tag{16}$$

In the aforementioned equation, $\hat{n}$ is the unit vector in the direction of anisotropy. Using the above relation, the interaction term of quarks in Eq. (9) is modified, and hence, the distribution functions are obtained in an anisotropic medium. The anisotropy parameter is defined in terms of $p_\parallel$, the component of momentum parallel to $\hat{n}$ and $p_\perp$, the component of momentum perpendicular to $\hat{n}$ as $\xi = \frac{\langle p^2_\perp \rangle}{\langle 2p^2_\parallel \rangle} - 1$. The parameter ξ varies over the range $-1 < \xi < \infty$, signifying the degree and nature of momentum-space anisotropy. An isotropic momentum distribution is represented when ξ equals 0, and as ξ becomes greater than 0, the momentum distribution undergoes squeezing along the n direction. Conversely, $-1 < \xi < 0$ corresponds to a stretched momentum distribution along the n direction. In conjunction with heavy-ion collision experiments, opting for the direction of nucleon-nucleon collision as the n-axis is rational and practical. This parametrization facilitates the formulation of the dispersion relation for quarks and antiquarks as

$$E^{*(\mathrm{aniso})}_f = \sqrt{p^2 + \xi p^2 \cos\theta^2 + m^{*2}_f}. \tag{17}$$

The expression of total thermodynamic potential in anisotropic quark matter is obtained by redefining the effective energy of condensates and substituting the above relation in Eq. (7). The impact of the finite size on the thermodynamic properties can be investigated using lower momentum cutoff or boundary conditions. Following the Refs. [23,35,90], in the present manuscript, the finite size effects are introduced by a lower momentum cutoff, denoted as $p_{\min}$ [MeV], equal to π/R [MeV], where R

signifies the length of a cubic volume. This lower momentum cutoff has been introduced in Eq. (11) by replacing $\vec{p}=0$ by π/R. This term gives the thermal contribution of quarks and thus gets modified due to the introduction of a lower momentum cutoff. As discussed in Ref. [91], when quantum field theory is applied to finite temperatures, an imaginary time parameter has to be introduced, varying from $\tau=0$ to $\tau=-\mathrm{i}\beta$. In the imaginary time formalism, the energy component attains discrete values due to finite τ values. In a similar manner, the implication of finite size discretizes the four-momentum component, $(p_0,\vec{p})$ applying, $p_0\to\frac{2\pi}{\beta}(\mathrm{n}+\frac{1}{2})$ and $\vec{p}\to\frac{2\pi}{R}(\mathrm{n}+\mathrm{c})$, here, $\mathrm{n}=0,\pm1,\pm2\ldots$ and $\mathrm{T}=1/\beta$. Here, $c=0$ and $1/2$ corresponds to periodic and anti-periodic boundary conditions, respectively. The Kubo-Martin-Schwinger conditions necessitate the implication of antiperiodic boundary conditions in imaginary-time coordinates due to the fermionic nature of the system under investigation [92–94]. However, for spatial coordinates, there are no restrictions on which boundary conditions should be taken into account [95–97]. As described in Ref. [28], by employing the technique of analytic continuation, the discrete sum of energies can be written as a continuous integral over momentum states. In the case of three momentum components, approximating the discrete sum as a continuous integration commences from the lower momentum cutoff. By analyzing a one-dimensional boson gas, the authors in Ref. [98] have highlighted that the inclusion of finite size corrections by the introduction of lower momentum cutoff correctly reproduces the thermodynamic properties. For simplification, the curvature and surface effects are not considered in the current work.

The equations of motion for scalar, vector, and the Polyakov loop fields are derived by minimizing the total thermodynamic potential as

$$\frac{\partial\Omega}{\partial\sigma_u}=\frac{\partial\Omega}{\partial\sigma_d}=\frac{\partial\Omega}{\partial\sigma_s}=\frac{\partial\Omega}{\partial\omega}=\frac{\partial\Omega}{\partial\rho}=\frac{\partial\Omega}{\partial\phi}=\frac{\partial\Omega}{\partial\Phi}=\frac{\partial\Omega}{\partial\bar{\Phi}}=0. \qquad (18)$$

The field equations are thus utilized to obtain values of quark condensates and vector fields [70]. Using the total thermodynamic potential calculated in Eq. (7), pressure density is calculated by the relation $p=-\Omega$. Further, the fluctuations of conserved charges are calculated by Taylor's series expansion method at the zero value of the corresponding chemical potential. The susceptibilities of order n_{th} are written as

$$\chi^{qIS}_{ijk}=\frac{\partial^{i+j+k}[p/T^4]}{\partial(\mu_q/T)^i\partial(\mu_I/T)^j\partial(\mu_S/T)^k}. \qquad (19)$$

The given series is expanded for chemical potential value zero, and hence susceptibilities are obtained for varying temperature values at $\mu_q=\mu_S=\mu_I=0$ in the current work. The value of the susceptibilities is dependent on the value of the vector-interaction constant as well as the Polyakov loop under consideration [70].

III. RESULTS AND DISCUSSION

In this section, we discuss the effect of the finite system size, R, strangeness chemical potential, μ_S, and momentum anisotropy on the thermodynamics of isospin asymmetric quark matter. It has been pointed out in earlier studies that the determination of the parameters of the model is dependent on the inclusion of vacuum mesonic fluctuations term [87]. The expectation values of curvature mass and sigma field are used as input to calculate the sigma-meson mass, m_σ, and pion decay constant, f_π [99]. The strength of vector coupling is determined by the coupling constant, g_v, defined as $v=g_v/g_s$.

The introduction of vector interactions has been found to impact the position of the QCD endpoint in the mean-field as well as in the functional renormalization group (FRG) approach [69,70]. In FRG, enhancing the repulsive vector interaction has shifted the critical endpoint (CEP) toward high temperature and lower chemical potential values in the two-flavor quark meson model [69]. The extension of the quark meson model with the inclusion of Polyakov loop variables, along with the introduction of vector interactions, helps in giving a comprehensive description of the strong interaction dynamics, enriching our understanding of the phase structure and properties of strongly interacting matter under varying conditions. The model parameters in the current work are taken from Ref. [87]. Also, a finite value of isospin chemical potential is anticipated in heavy-ion collision. Thus, it becomes important to include isospin asymmetry when studying the thermodynamic properties of quark matter.

In Sec. III A, the phase diagram and CEP are analyzed for varying system sizes and strangeness chemical potential values for isotropic momentum distribution. Section III B highlights the results of varying momentum anisotropy parameter ξ on susceptibilities of conserved charges and phase transitions. In the later discussion of current work, the strangeness chemical potential values have been taken, ranging from positive to negative, to study the regimes of finite strangeness created due to fluctuations [59,100,101]. It has been investigated by Greiner *et al.* in [101] that strangeness separation occurs within the Gibbs-phase coexistence of a baryon-rich quark-gluon plasma and hadron matter, even when the temperature is zero ($\mathrm{T}=0$). This separation happens because the system becomes energetically favorable when s quarks remain in the quark phase. As the temperature rises to a finite value, the strange K mesons containing s quarks are produced in the hadron phase while the s quarks reside within strange-quark-matter droplets. Also, in the analysis of data from nucleus-nucleus collisions at the AGS and SPS, it has been suggested that a distinct and straightforward indication of the transition from hadronic matter to quark-deconfined matter is the alteration of the sign of the strange-quark chemical potential [102,103] which is dependent on strangeness chemical potential as defined in Eq. (15). The authors in [59] have shown the abundance of s quarks as the strangeness chemical potential tends to be more negative in the chiral parity doublet model framework.

Similarly, the baryonic chemical potential values are varied over a range to investigate the behavior of quark matter in extreme conditions. The infinite value of R corresponds to infinite system size, whereas to consider finite volume conditions, $R = 5$, 3 fm is taken by employing a lower momentum cutoff. Studying the quark matter in isotropic and anisotropic finite volume by considering a finite value of strangeness chemical potential, temperature, baryonic chemical potential, and vector and scalar interactions helps to recreate a more well-defined system to investigate the QCD phase transitions and critical endpoint.

A. Impact of finite volume and strangeness chemical potential in isotropic medium

In this section, the effect of finite system volume and strangeness chemical potential on isotropic matter is investigated. The value of the vector coupling constant has been fixed at $g_v = 6.5$ with $v = 1$, and the isospin chemical potential, $\mu_I = 30$ MeV. As discussed in the introduction, finite values of isospin and strangeness chemical potentials have been interpreted in HICs, necessitating the evaluation of field configurations and thermodynamic quantities under these nonzero potentials [51]. In Fig. 1 we have shown the variation of u quark condensate, σ_u/σ_{u0}, (normalized with respect to vacuum value of u quark condensate, σ_{u0}), as a function of the baryonic chemical potential, μ_B for $R = \infty$, 5 and 3 fm, and the strangeness chemical potential ranging from positive to negative values, for temperatures, $\mathrm{T} = 30$ and 60 MeV whereas Fig. 2 shows these results at $T = 100$ and 150 MeV. We have observed a sudden decrease in the value of the quark condensate with increasing μ_B, which signifies the phase change at higher chemical potential for all values of μ_S and R. For decreasing volume and at a given value of μ_S, this change in chiral condensate values occurs at a higher value of μ_B.

On the contrary, for a given system size and temperature, a drop in σ_u/σ_{u0} at lower baryonic chemical potential values for decreasing μ_S is observed. Hence, the critical chemical potential is found to be shifted toward higher values for decreasing system volume and increasing strangeness chemical potential. As the temperature increases from low to high values, the u quark condensate drops significantly. For $\mathrm{T} = 150$ MeV and infinite system size, $\sigma_u/\sigma_{u0} < 0.2$ for all values of μ_B and μ_S. The decrease in the value of the quark condensate with an increase in the value of temperature signifies the phase change from confined to a deconfined state. As stated by Eq. (14), condensate σ_u is directly proportional to the effective mass of u quark. Hence, the variation of m_u^* follows the same trend as σ_u with a change in system size and strangeness chemical potential. The value of quark condensate has been found to increase with increasing the strength of vector coupling, g_v at a given value of baryon chemical potential, whereas it decreases with increasing the isospin chemical potential, μ_I [70]. The authors in Ref. [104] have observed that increasing the isospin chemical potential value shifts the transition temperature to a lower value, evident from the behavior of the pseudo-critical temperature and quark condensates. These changes in vector interaction coupling and isospin chemical potential have been found to have an opposite impact on phase transition, as has also been observed in Refs. [77,105]. Thus, increasing μ_I favors the restoration of chiral symmetry, whereas increased vector coupling tends to delay the same.

As discussed earlier, in the current work, the finite volume effect is included by applying a lower momentum cutoff, i.e., π/R, only to the quark interaction term and not to the mesonic vacuum term in Eq. (10). The authors in Ref. [106] have shown that due to the inclusion of finite size effect in the mesonic vacuum fluctuation term, the chiral phase transition line shows an opposite trend. Though the CEP moves to low T and high μ_q with decreasing system size, the chiral phase transition line shifts to a lower value of temperature and quark chemical potential. Also, the value of nonstrange quark condensate shows a similar trend as the present work with vacuum term defined by infinite system size, whereas for the finite size incorporated vacuum term, the value of nonstrange quark condensate decreases with decreasing system size. This shows that there is an early onset of chiral symmetry restoration for lower system sizes with finite volume vacuum term in contradiction to delayed restoration of chiral symmetry for infinite size vacuum term. Due to the change in the value of quark condensate, the masses of the quarks change as a function of system volume. A sharp drop in the mass of u quark condensate with decreasing system size has been reported in Ref. [107] in the PNJL model, which includes the vacuum fluctuations. In the framework of the PQM model with no vector interactions [106], and consideration of discrete boundary conditions for momentum causes a significant change in the trajectory of CEP, and as a consequence, the obtained finite volume effects are inconclusive. However, the NJL model in the mean-field approximation and Schwinger conditions was employed to study the solution of the gap equation and chiral susceptibilities in finite size effects by taking into account the different boundary conditions [96].

The deconfinement transition is well explained by Polyakov loop parameters, Φ and $\bar{\Phi}$. Thus, the derivatives of the chiral condensates and the Polyakov loop parameters are calculated to study the QCD phase diagram and, hence, plot the chiral phase transition boundary and the deconfinement transition line, respectively. The first-order phase transition line ends at a critical point and becomes a

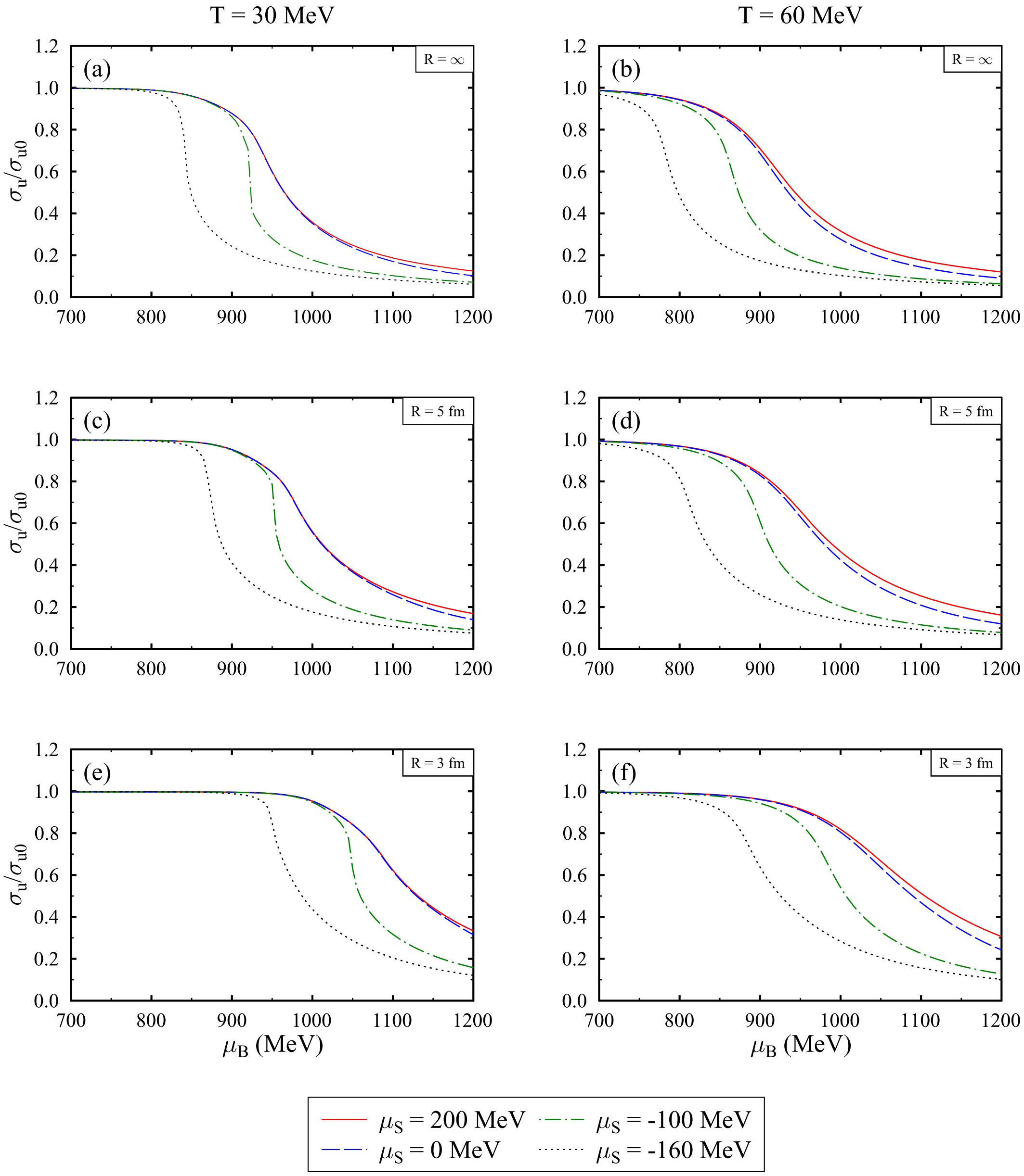

FIG. 1. The u quark condensate, σ_u/σ_{u0} (normalized with respect to vacuum value of u quark condensate, σ_{u0}) plotted as a function of baryon chemical potential, μ_B, for strangeness chemical potential, $\mu_S = 200$, 0, -100, and -160 MeV,. Results are shown for system size $R = \infty$ [in subplots (a) and (b)], 5 fm [in subplots (c) and (d)], and 3 fm [in subplots (e) and (f)] and temperatures T $= 30$ MeV [in subplots (a), (c) and (e)], and 60 MeV [in subplots (b), (d) and (f)].

crossover for the chiral limit [108]. The deconfinement transition line remains a crossover for all the values of temperature. The first-order phase transition line is deduced by plotting the susceptibility of the chiral condensate as a function of baryonic chemical potential at a fixed temperature value. This is because the first-order phase transitions involve a discontinuous change in the order parameter at the transition point. On the other hand, crossover represents a gradual change in physical properties as a function of temperature or other parameters. The susceptibility does not diverge at crossover; instead, it remains finite [108–110].

The nature of the phase transition from confined to deconfined state with increasing μ_B is more accurately predicted through derivatives of the strange and nonstrange quark condensates. In Fig. 3, the variation in vector density, ρ_u, and susceptibility, χ_u of u quark has been shown as a function of the baryonic chemical potential for $R = 5$ and 3 fm at $\mu_S = 200$, 0, -100 and -160 MeV. The sharp rise in susceptibility values at low temperatures suggests a first-order phase transition, while the smooth change signals the crossover. It is clear from Figs. 3(a) and 3(c) that the critical value of the baryonic chemical potential moves to a lower

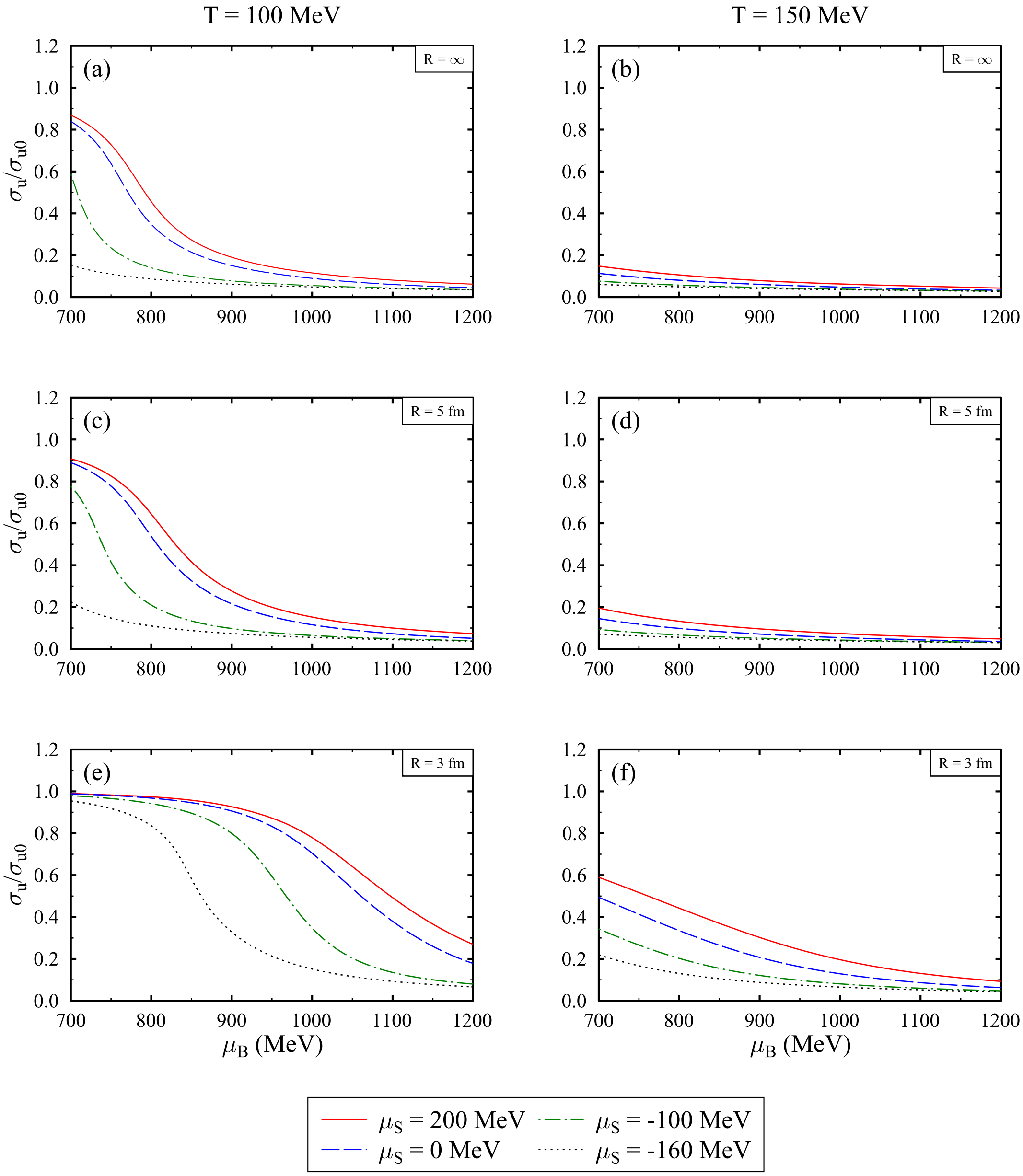

FIG. 2. The u quark condensate, σ_u/σ_{u0} (normalized with respect to vacuum value of u quark condensate, σ_{u0}) plotted as a function of baryon chemical potential, μ_B, for strangeness chemical potential, $\mu_S = 200$, 0, -100, and -160 MeV. Results are shown for system size $R = \infty$ [in subplots (a) and (b)], 5 fm [in subplots (c) and (d)], and 3 fm [in subplots (e) and (f)] and temperatures $T = 100$ MeV [in subplots (a), (c), and (e)], and 150 MeV [in subplots (b), (d), and (f)].

value at finite μ_S and Figs. 3(b) and 3(d) shows the shift to higher μ_B for decreasing volume. The sharp peak in the susceptibility of the u quark, at T = 30 MeV, confirms the first-order phase transition. The susceptibility peak smoothens with increased temperature values, indicating a crossover transition. The change in the phase transition line from crossover to first-order phase transition at varying values of μ_S and R is highlighted by the peak of χ_u. The curve becomes smoother, and very little change is observed at T = 120 MeV for all values of R and μ_S, highlighting the crossover regime. It has been observed that the peak of χ_u shifts to a higher baryonic chemical potential for increasing vector coupling strength for a given value of μ_S, T, and R, whereas there is an opposite shift to lower value of μ_B with increasing isospin chemical potential. This result is deduced from the behavior of u quark condensate with varying g_v and μ_I, which is discussed earlier in this section.

Figure 4 shows the dependence of the strange quark vector density, ρ_s, and susceptibility, χ_s, on the variation of strangeness chemical potential and system size at different temperatures. For vanishing μ_S and given system size, ρ_s is almost zero for $\mu_B \approx 1050$ MeV and T = 30 MeV. This shows that strange quarks are produced at the higher baryonic chemical potential for the vanishing value of

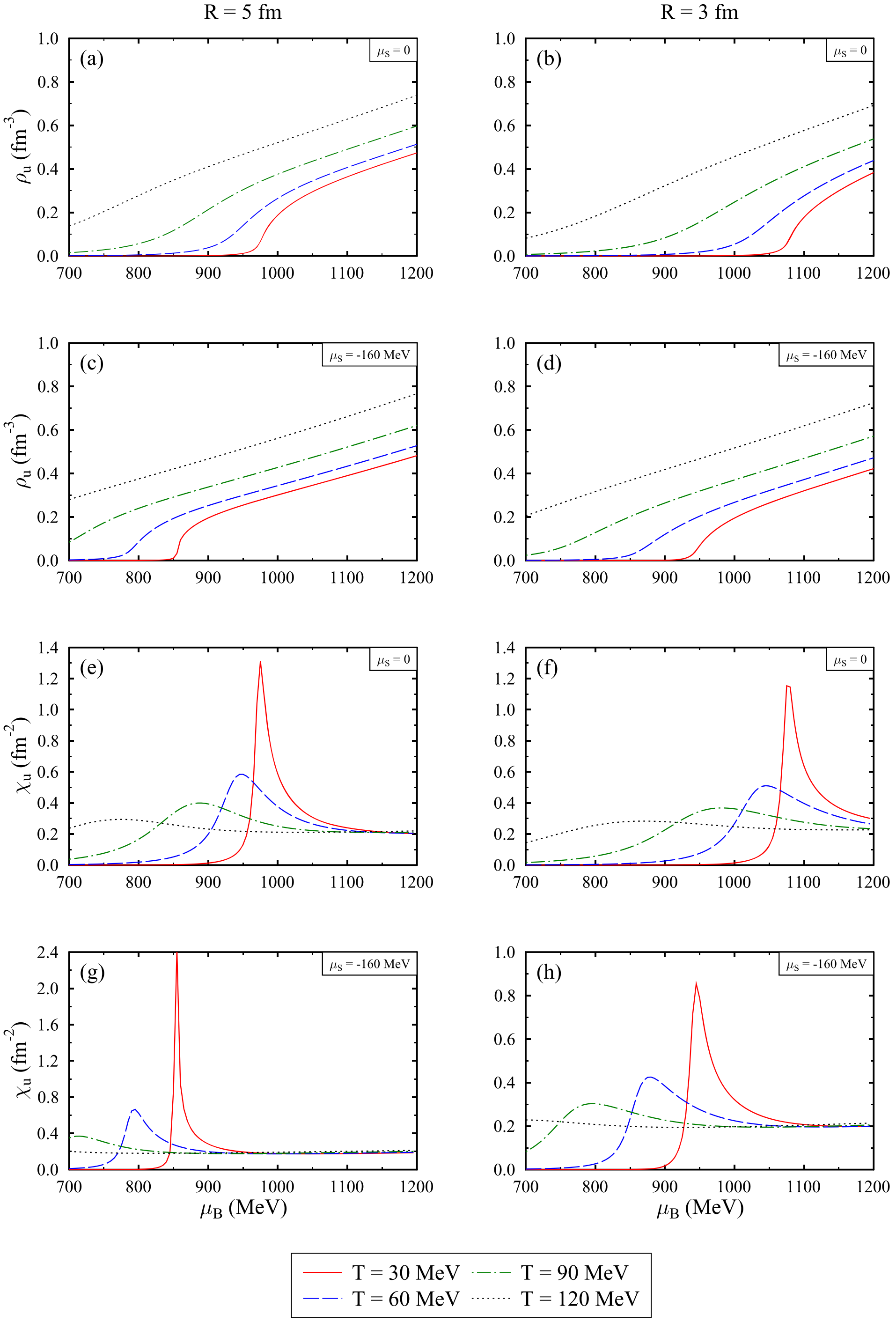

FIG. 3. The u quark density, ρ_u, and susceptibility, χ_u plotted as a function of baryon chemical potential, μ_B for temperature, T = 30, 60, 90, 120 MeV. Results are shown for system size $R = 5$ fm [in subplots (a), (c), (e), and (g)], and 3 fm [in subplots (b), (d), (f), and (h)] and strangeness chemical potential, $\mu_S = 0$ [in subplots (a), (b), (e), and (f)], and -160 MeV [in subplots (c), (d), (g), and (h)].

strangeness chemical potential. With the increasing value of T and μ_B, ρ_s shows a monotonically increasing trend. For the finite value of μ_S, the density of s quarks in the system remains zero for finite μ_B, and then a sudden change is observed at fixed volume. This sudden rise may signify the change in phase from a confined to a deconfined state. For high-temperature values, ρ_s increases uniformly with μ_B. The increase in density of s quarks is observed to occur at a higher μ_B for $R = 3$ fm at a given temperature and strangeness chemical potential value. Compared to the u quark susceptibility in Fig. 3, no peak is observed for the vanishing value of μ_S at T = 30 MeV. Hence, the phase transition line of s quark is a crossover at low-temperature values for given system sizes and for zero value of μ_S, which indicates that the

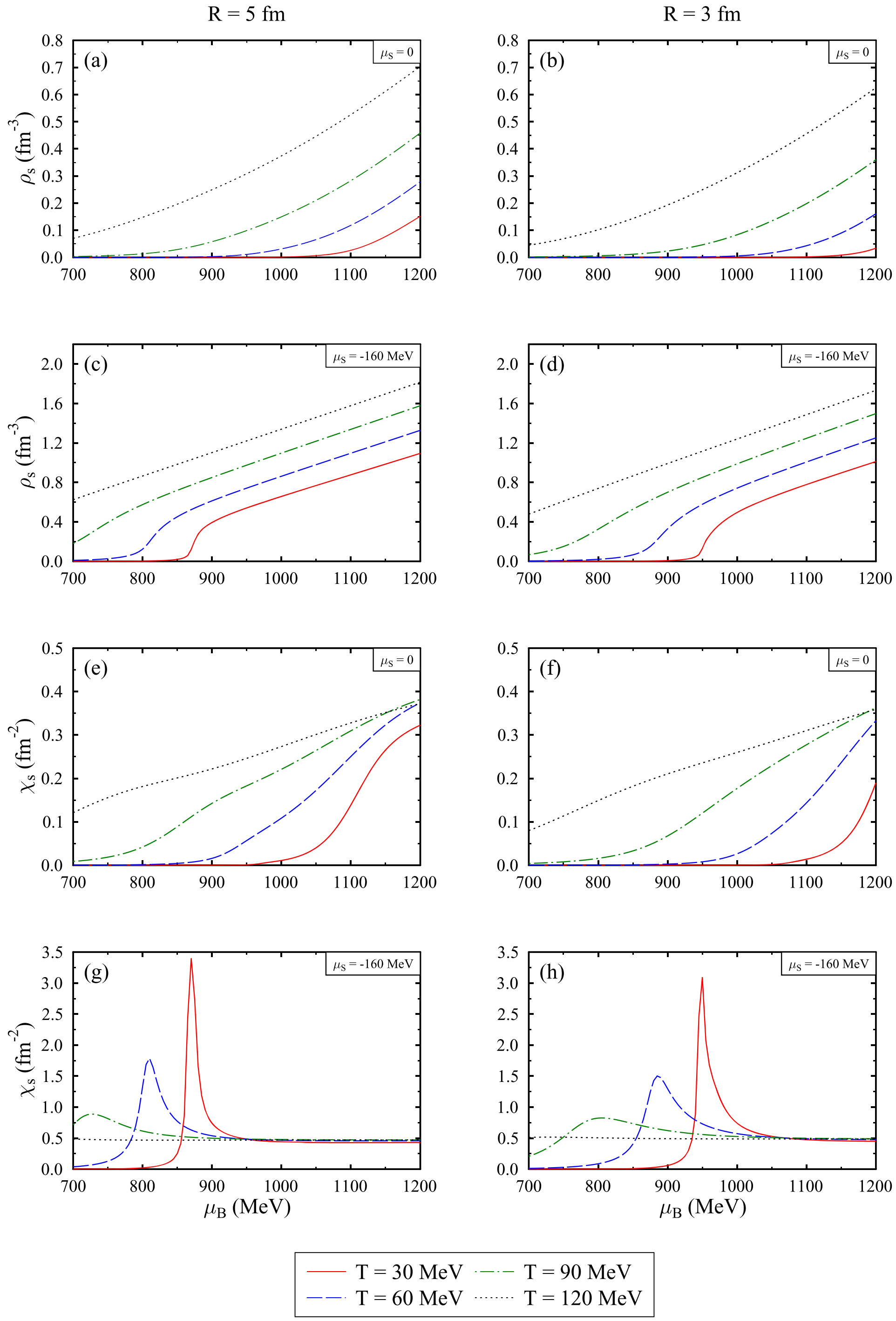

FIG. 4. The strange quark density, ρ_s, and susceptibility, χ_s plotted as a function of baryon chemical potential, μ_B for temperature, $T = 30$, 60, 90, 120 MeV. Results are shown for system size $R = 5$ fm [in subplots (a), (c), (e), and (g)], and 3 fm [in subplots (b), (d), (f), and (h)] and strangeness chemical potential, $\mu_S = 0$ [in subplots (a), (b), (e), and (f)], and -160 MeV [in subplots (c), (d), (g), and (h)].

phase transition line of strange quarks might not coincide with nonstrange quarks at low-temperature values and vanishing strangeness chemical potential. The appearance of the peak in the χ_s at $T = 30$ and 60 MeV for both the given system volumes emphasizes the shift of critical temperature to a higher point in the QCD phase diagram.

Figure 5 shows the derivatives of chiral strange and nonstrange condensates and Polyakov loop variables with varying temperature values for a given quark chemical potential. The peak of the plotted derivatives of order parameters gives the value of critical temperature at a given value of chemical potential. For the vanishing value of μ_S,

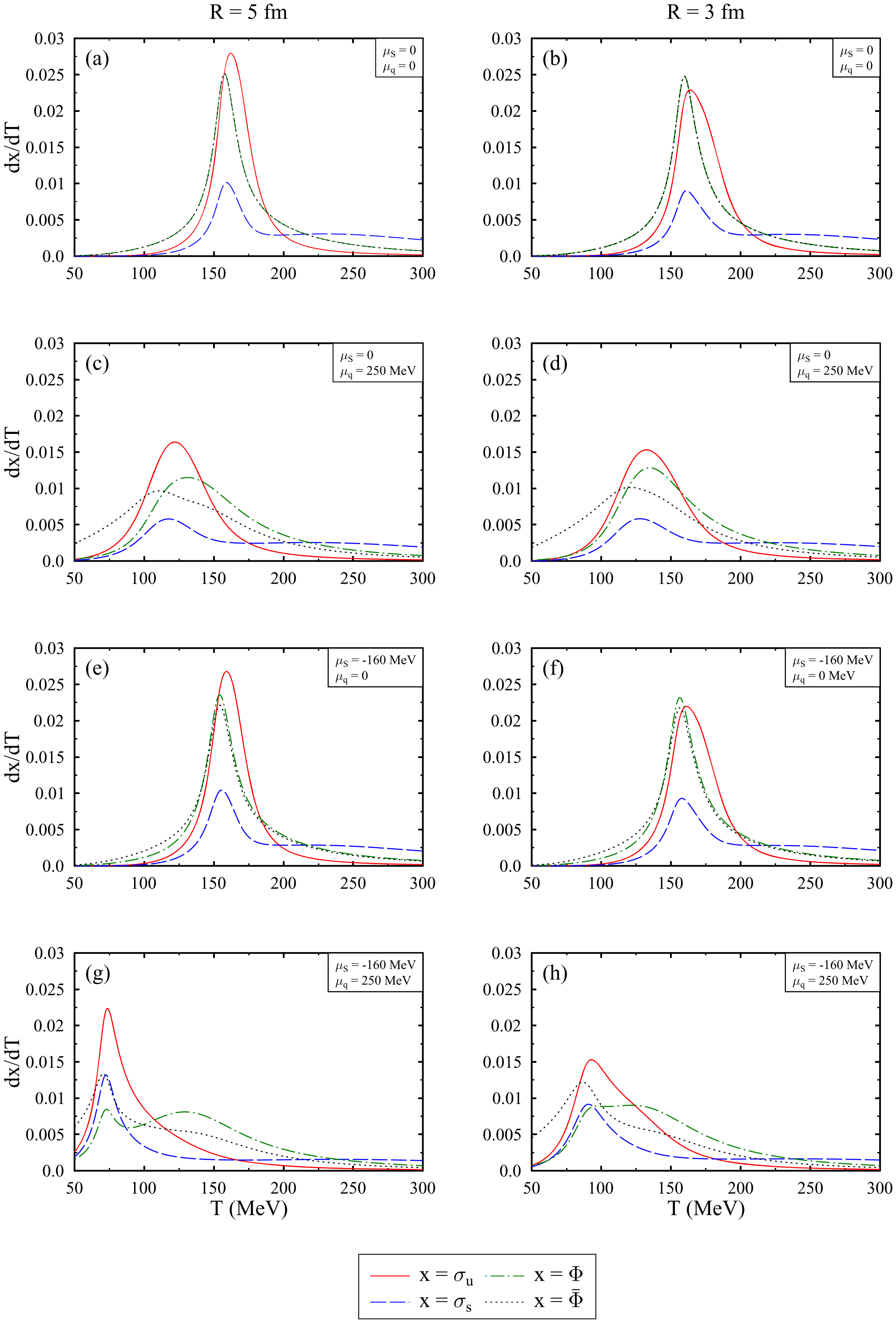

FIG. 5. The derivatives of quark condensates and Polyakov loop variables plotted as a function of temperature, T for quark chemical potential, $\mu_q = 0$ [in subplots (a), (b), (e), and (f)] and 250 MeV [in subplots (c), (d), (g), and (h)]. Results are shown for system size $R = 5$ fm [in subplots (a), (c), (e), and (g)], and 3 fm [in subplots (b), (d), (f), and (h)] and strangeness chemical potential, $\mu_S = 0$ [in subplots (a), (b), (c), and (d)], and -160 MeV [in subplots (e), (f), (g), and (h)].

there are only single peaks in the derivatives of chiral condensates and Polyakov loop parameters. For the zero value of μ_q, the curve for Φ coincides with that of $\bar{\Phi}$ as these parameters have equal values in this confined regime. The shift of peaks for different values of μ_S and system size is the same as discussed earlier. For the finite value of μ_S and μ_q,

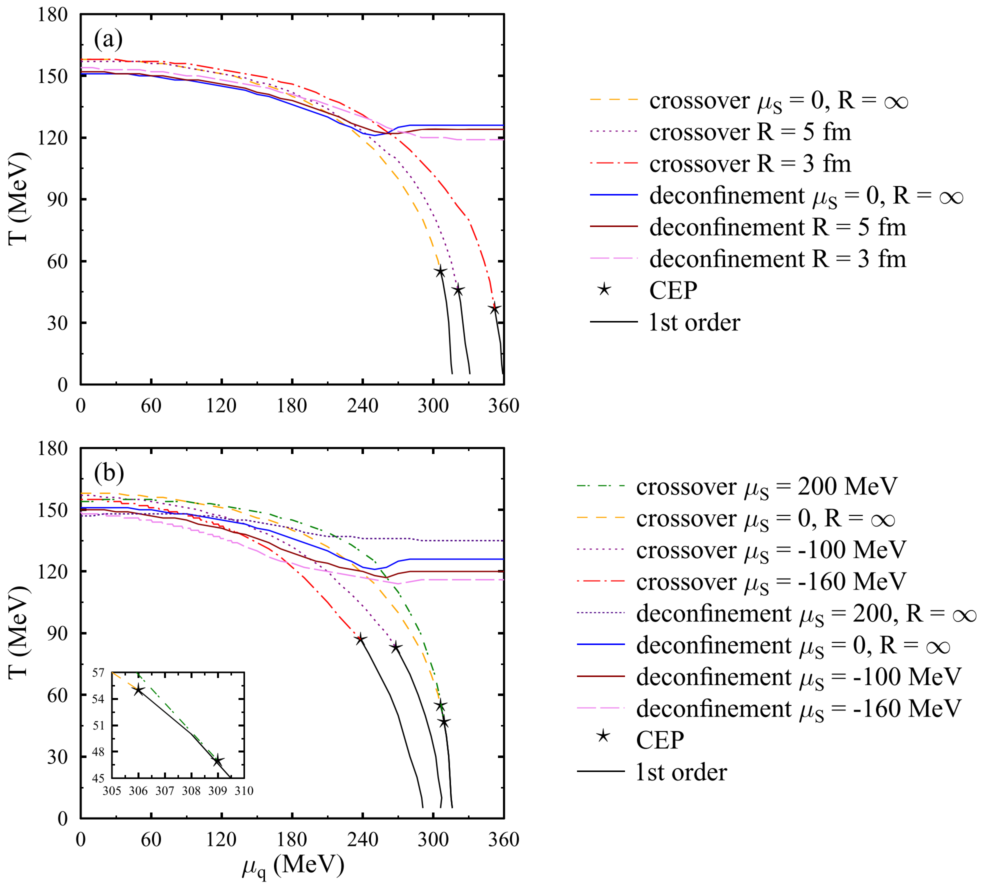

FIG. 6. The QCD phase diagram for varying system sizes, $R = \infty$, 5, and 3 fm [in subplot (a)] and strangeness chemical potential, $\mu_S = 200$, 0, -100, and -160 MeV [in subplot (b)], for vector coupling constant, $g_v = 6.5$.

two peaks are observed for Φ. In this scenario, the critical point is calculated by using the condition $\Phi(\mathrm{T})/\Phi(T \to \infty) > 1/2$ [111]. In comparison to the density derivatives plotted in Figs. 3 and 4, the peak of derivatives in this case is smoother and does not diverge at the critical point. Thus signifying the existence of a crossover in this scenario.

Using the critical temperature values derived from Figs. 4 and 5, the QCD phase diagram for different system sizes and strangeness chemical potential has been displayed in Fig. 6. The chiral phase boundary and the deconfinement transition line have been shown for $R = \infty$, 5 and 3 fm and $\mu_S = 0$ in the above panel while for $\mu_S = 200$, 0, -100 and -160 MeV and $R = \infty$ in the below panel. At the critical point, the first-order phase transition changes to the crossover for the chiral phase transition. The position of the critical point at the vanishing value of μ_S and infinite size is $(\mu_{q(CP)}, T_{CP}) = (306, 55)$ MeV. For $R = 5$ fm, the critical value of the temperature drops by 16.37% and increases by 4.91% for quark chemical potential. A further drop of 19.57% for the critical temperature and a 9.66% increase in quark chemical potential value is observed for $R = 3$ fm. For the positive value of μ_S, it should be noted that the first-order phase transition line almost overlaps that of $\mu_S = 0$, but T_{CP} falls by 14.5%, while $\mu_{q(CP)}$ changes positively by only 0.9%. This can also be observed in the trends of u quark condensate in Fig. 1, where a negligible change is observed at $\mathrm{T} = 30$ and 60 MeV with increasing μ_B. For $\mu_S = -100$ MeV, the critical temperature rises by 50.9% whereas $\mu_{q(CP)}$ falls by 12.42%. For $\mu_S = -160$ MeV, critical quark chemical potential decreases by 11.2%, whereas T_{CP} increases further by 4.81%. Hence, from the above discussion, it is clear that the critical point shifts to a lower temperature value and higher quark chemical potential with decreasing system size. A similar change in the value of the critical point has also been observed in the Polyakov loop modified Nambu-Jona-Lasinio (NJL) model [20,35], though an opposite change to a higher temperature for the critical point has also been reported with a decrease in volume in the framework of Polyakov chiral quark mean field model [34].

As the value of μ_S approaches the negative value, the phase boundary becomes a first-order phase transition with increasing T_{CP} and decreasing $\mu_{q(CP)}$. The change in the phase transition order at finite μ_S with increasing temperature has also been highlighted in [58,112]. The values of the critical points for varying volume and strangeness chemical potential have been listed in Table I. The deconfinement boundary remains crossover for all temperatures and quark chemical potential values for all R and μ_S. A very small shift

TABLE I. The value of critical temperature and quark chemical potential for finite values of system size and strangeness chemical potential.

R value	$R = \infty$	$R = 5$ fm	$R = 3$ fm	$R = \infty$	$R = \infty$	$R = \infty$
μ_S value	$\mu_S = 0$	$\mu_S = 0$	$\mu_S = 0$	$\mu_S = 200$ MeV	$\mu_S = -100$ MeV	$\mu_S = -160$ MeV
T_{CP} (MeV)	55	46	37	47	83	87
$\mu_{q(CP)}$ (MeV)	306	321	352	309	268	238

to lower values is observed for the deconfinement transition temperature for reduced system volume and negative values of strangeness chemical potential.

Fluctuations and susceptibilities of conserved charges have been recognized as observables, which helps to find the location and nature of the QCD critical point. Figures 7 and 8 shows the second-order susceptibility and kurtosis of quark number and strangeness number for varying values of system volume and μ_S. The susceptibilities have been calculated using Taylor's series expansion method for vanishing values of corresponding chemical potentials. In Figs. 7(a) and 7(c), for zero value of μ_S and changing system size, χ_2^q and χ_4^q/χ_2^q changes rapidly near the transition regime. There is a slight shift in the critical temperature value to a higher temperature with decreasing system size. But as discussed earlier, for finite values of μ_q, the critical temperature shifts toward lower values for a reduced system volume. On the other hand, for finite values of μ_S and infinite system size, the critical temperature is shifted to a lower value for decreasing μ_S, which contrasts with results discussed at finite μ_q. The kurtosis value drops nearly to zero for higher temperatures, which signifies the change in degrees of freedom to quarks. The value of second-order susceptibility for quarks increases monotonically with the rise in temperature in both scenarios. The critical temperature for zero value of μ_q appears to be around 155 MeV, which coincides with the results of lattice QCD [113]. The value of susceptibilities depends on the form of the Polyakov loop under consideration and vector interactions. The comparison of these fluctuations of conserved charges with lattice data for changing g_v and the Polyakov loop has been discussed in earlier work for the zero value of μ_S and infinite volume [70].

The trend of second-order susceptibility of strangeness number is similar to that of χ_2^q. The kurtosis for the strangeness number shows a peak around the transition regime. The peak position is found to be shifted toward a lower temperature value for increasing system volume. This is similar to the change observed in the susceptibilities of quark number. While investigating the derivatives of the

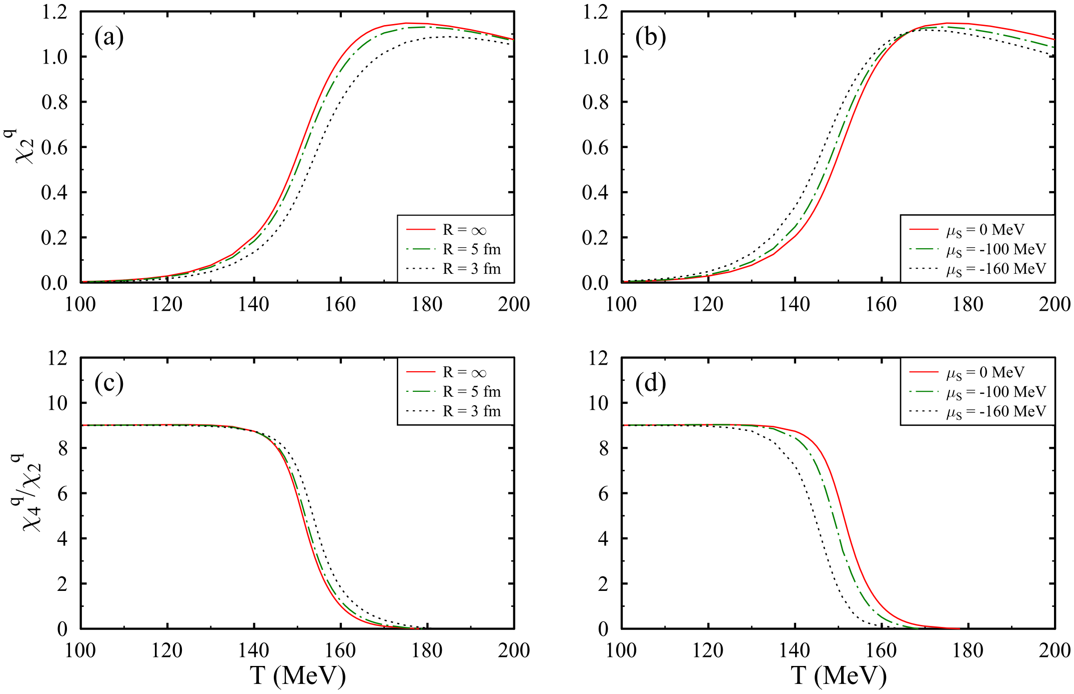

FIG. 7. The second order susceptibility, χ_2^q [in subplots (a) and (b)], and kurtosis, χ_4^q/χ_2^q [in subplots (c) and (d)], plotted as a function of temperature, T. Results are shown for system size $R = \infty$, 5, and 3 fm [in subplots (a) and (c)] and strangeness chemical potential, $\mu_S = 0$, -100, and -160 MeV [in subplots (b) and (d)].

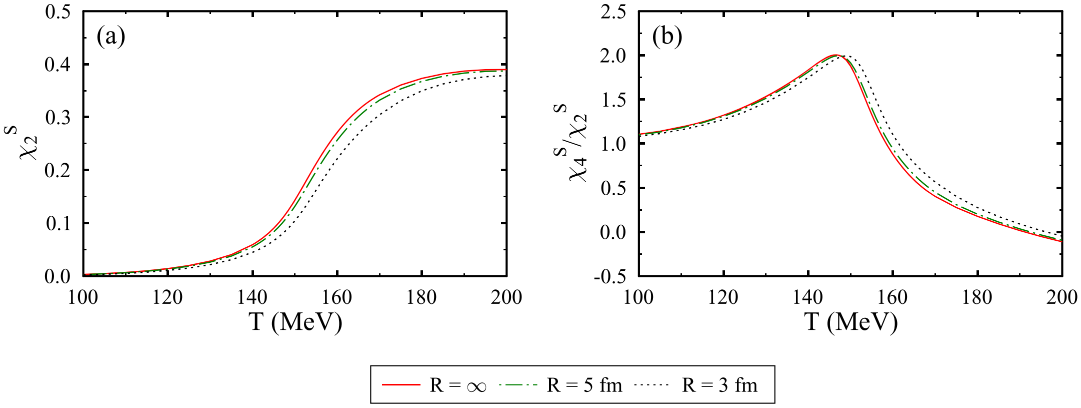

FIG. 8. The second-order susceptibility, χ_2^S [in subplot (a)], and kurtosis, χ_4^S/χ_2^S [in subplot (b)], plotted as a function of temperature, T and system size $R = \infty$, 5, and 3 fm.

chiral condensates, the change observed in critical temperature is opposite to that studied for finite chemical potential value.

B. QCD phase diagram for anisotropic momentum distribution

In this section, we discuss in detail the impact of the anisotropic distribution of momentum-space in finite-volume quark matter. When the value of the anisotropy parameter is small, it can be derived in terms of one-dimensional Bjorken expansion within the Navier-Stokes limit for a system resembling an ideal massless parton gas [114]. The expression for ξ is thus defined as $\xi = \frac{10}{T\tau}\frac{\eta}{s}$, where η is the shear viscosity, s is entropy density and τ represents the proper time of the medium [114]. Using the above expression, ξ is estimated to be around 0.3 for a relaxation time of 6 fm/c, the ratio $\eta/s = 1/4\pi$, and a critical temperature of 160 MeV at RHIC. Hence, by considering a very little deviation from the isotropic momentum space, the value of ξ is considered to be -0.2, 0.2, and 0.4 in current work. The isotropic momentum distribution is represented by $\xi = 0$, as in the Sec. III A. In order to study the change in critical point due to varying vector interactions, the value of $v = 0.5$ and hence vector coupling constant, $g_v = 3.25$, is taken. The value of μ_I is fixed at 30 MeV and strangeness chemical potential at $\mu_S = 200$ MeV for $R = \infty$ and 3 fm.

In Figs. 9 and 10, we have shown the variation of u quark condensate, σ_u/σ_{u0}, (normalized with respect to vacuum value of u quark condensate, σ_{u0}), strange quark condensate, σ_s/σ_{s0}, (normalized with respect to vacuum value of strange quark condensate, σ_{s0}) and Polyakov loop variables, Φ and $\bar{\Phi}$, as a function of temperature, T respectively. The order parameters are investigated for different values of the anisotropy parameter, ξ, and value of $R = \infty$ and 3 fm for quark chemical potential values fixed at 0 and 300 MeV. For the vanishing value of quark chemical potential and both system sizes, σ_u/σ_{u0} and σ_s/σ_{s0} decrease continuously with the rise in temperature values for all values of ξ. With the increase in value of ξ, σ_u/σ_{u0}, and σ_s/σ_{s0} value increases for a given T and μ_q, their melting behaviors exhibit a smoother transition. This observation indicates that large deviations from the isotropic medium tend to postpone the restoration of chiral symmetry. In the case of finite μ_q, the transition appears to be happening at a lower value of temperature at a given value ξ. In Figs. 9(b) and 9(d), the value of condensates drops to a lower value as compared to those at finite volume and finite quark chemical potential. This is attributed to the fact that the chiral symmetry restoration happens at higher μ_q for decreasing system size, as concluded in the previous section. Thus, with increasing volume, we observe a sharp fall in σ_u/σ_{u0}, and σ_s/σ_{s0} with varying values of anisotropy parameter at higher μ_q. Contrary to the case of quark condensates, the value of Φ and $\bar{\Phi}$ increases continuously as a function of temperature in all scenarios. The swift rise in Polakov loop variables with increasing T signifies the transition of confined state to deconfinement QGP. For the vanishing value of quark chemical potential, the Φ and $\bar{\Phi}$ have equal values. With an increasing value of ξ and at a given μ_q, the transition temperature seems to shift to a higher T value. Thus, the deconfinement phase transition line may shift to the higher value of temperature for a given value of quark chemical potential with an increase in momentum anisotropy of the system.

As discussed earlier, the phase diagram is plotted by investigating the derivatives of order parameters of the model. Figure 11 illustrates the derivatives of quark condensates and Polyakov loop variables for different values of ξ, and vanishing quark chemical potential. The peak of the derivatives of order parameters determines the critical temperature at a given value of μ_q. Clearly, with an increased anisotropic parameter, the peak is shifted to a higher temperature value, signifying the change in the transition line to higher T values. The peak of the up and strange quark condensate derivative coincides at a given

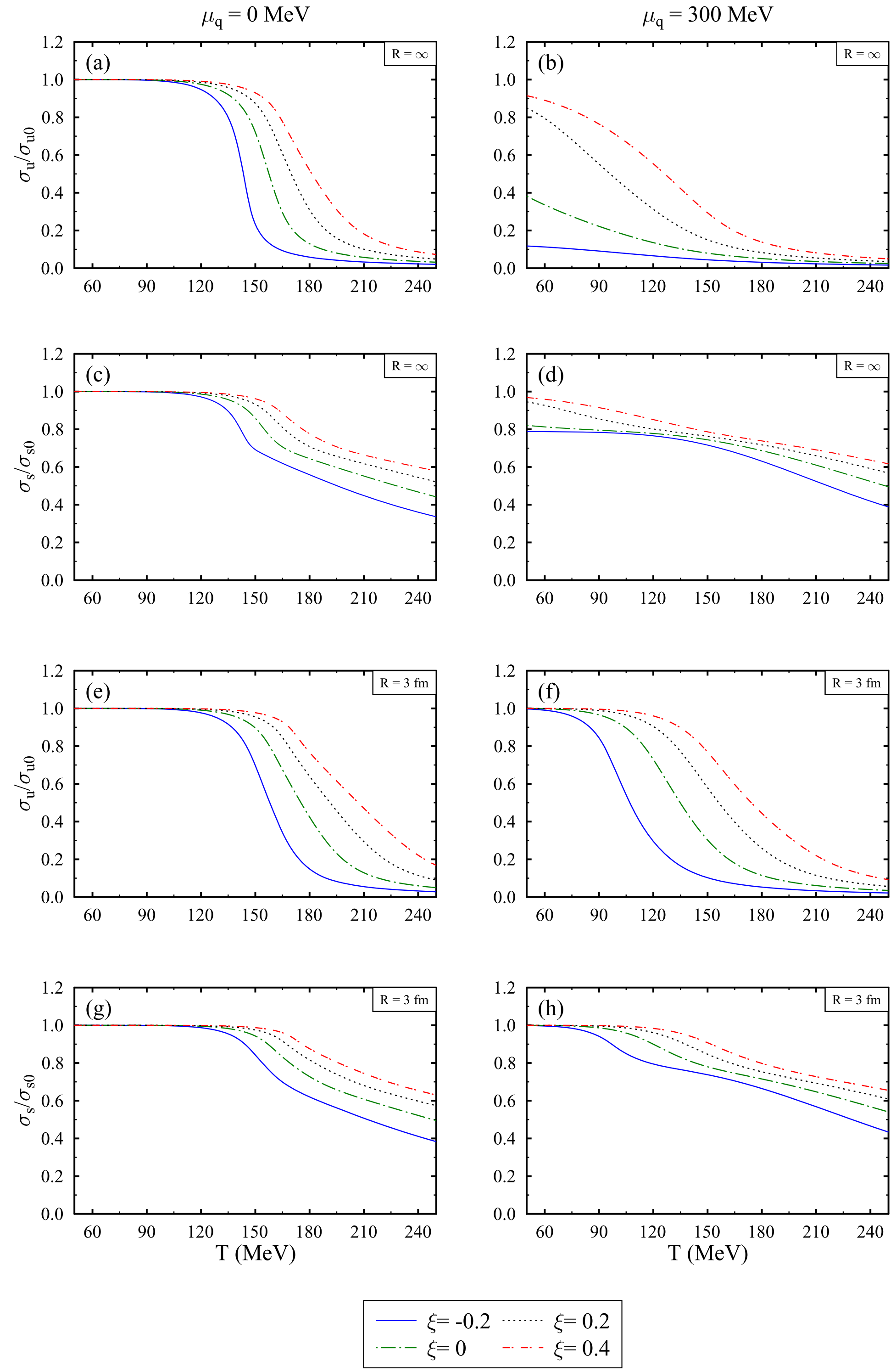

FIG. 9. The u quark condensate, σ_u/σ_{u0}, (normalized with respect to vacuum value of u quark condensate, σ_{u0}) and strange quark condensate, σ_s/σ_{s0}, (normalized with respect to vacuum value of strange quark condensate, σ_{s0}) plotted as a function of temperature, T, for anisotropy parameter, $\xi = -0.2$, 0, 0.2, and 0.4. Results are shown for system size $R = \infty$ [in subplots (a), (b), (c), and (d)], and 3 fm [in subplots (e), (f), (g), and (h)] and strangeness chemical potential, $\mu_q = 0$ [in subplots (a), (c), (e), and (g)], and 300 MeV [in subplots (b), (d), (f), and (h)].

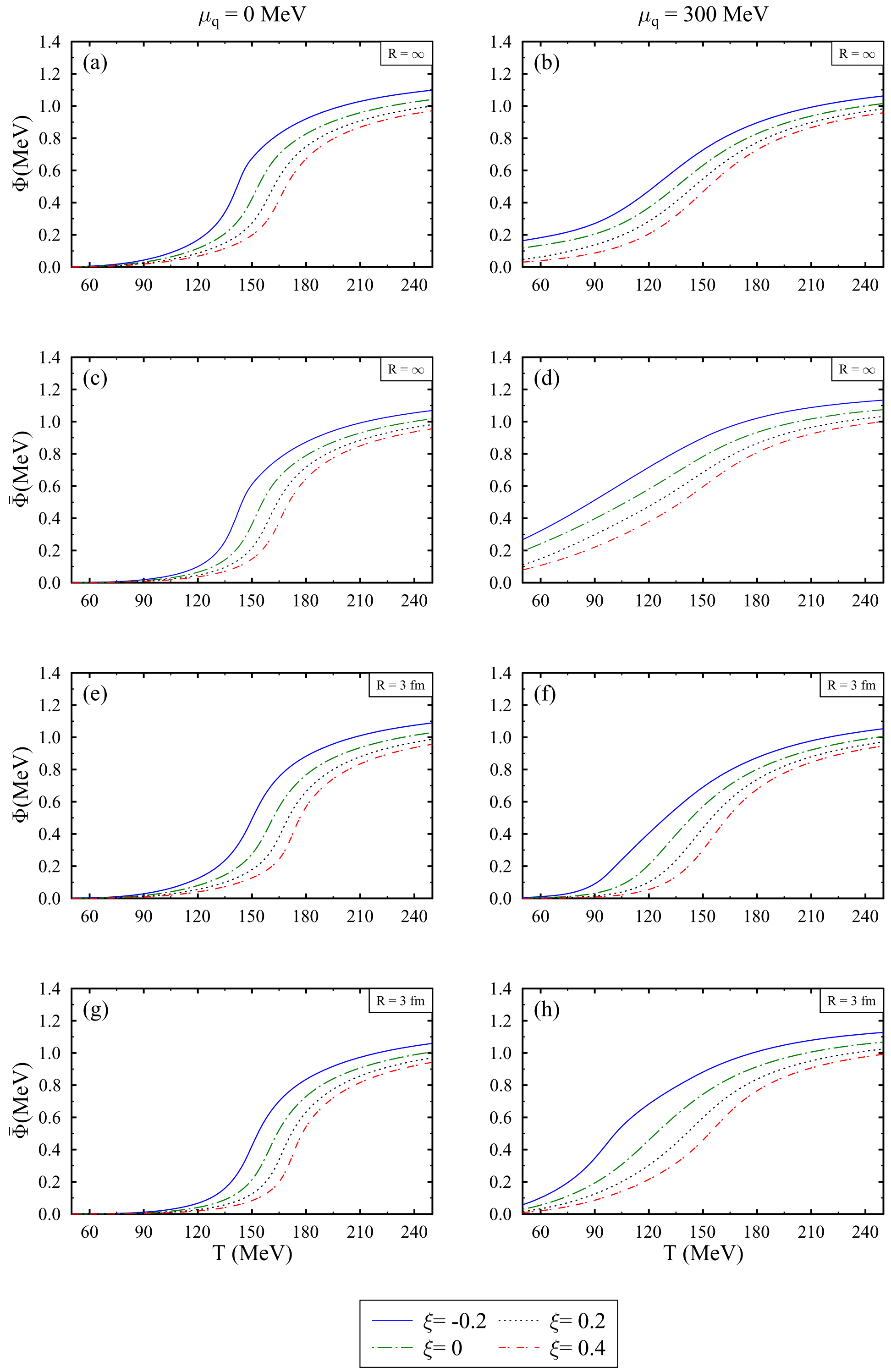

FIG. 10. The Polyakov loop variables Φ and $\bar{\Phi}$ plotted as a function of temperature, T, for anisotropy parameter, $\xi = -0.2$, 0, 0.2, and 0.4. Results are shown for system size $R = \infty$ [in subplots (a), (b), (c), and (d)], and 3 fm [in subplots (e), (f), (g), and (h)] and strangeness chemical potential, $\mu_q = 0$ [in subplots (a), (c), (e), and (g)], and 300 MeV [in subplots (b), (d), (f), and (h)].

value of ξ, showing the overlap of the strange and non-strange chiral boundary. A similar shift of peak to higher T values is observed for Polaykov loop variables with increasing ξ. The shift of the critical point to a lower T value, with increasing system size, at a given value of ξ demonstrates the change in the phase transition line. Using the following derivatives and determining the critical temperature for varying μ_q, the phase diagram showing

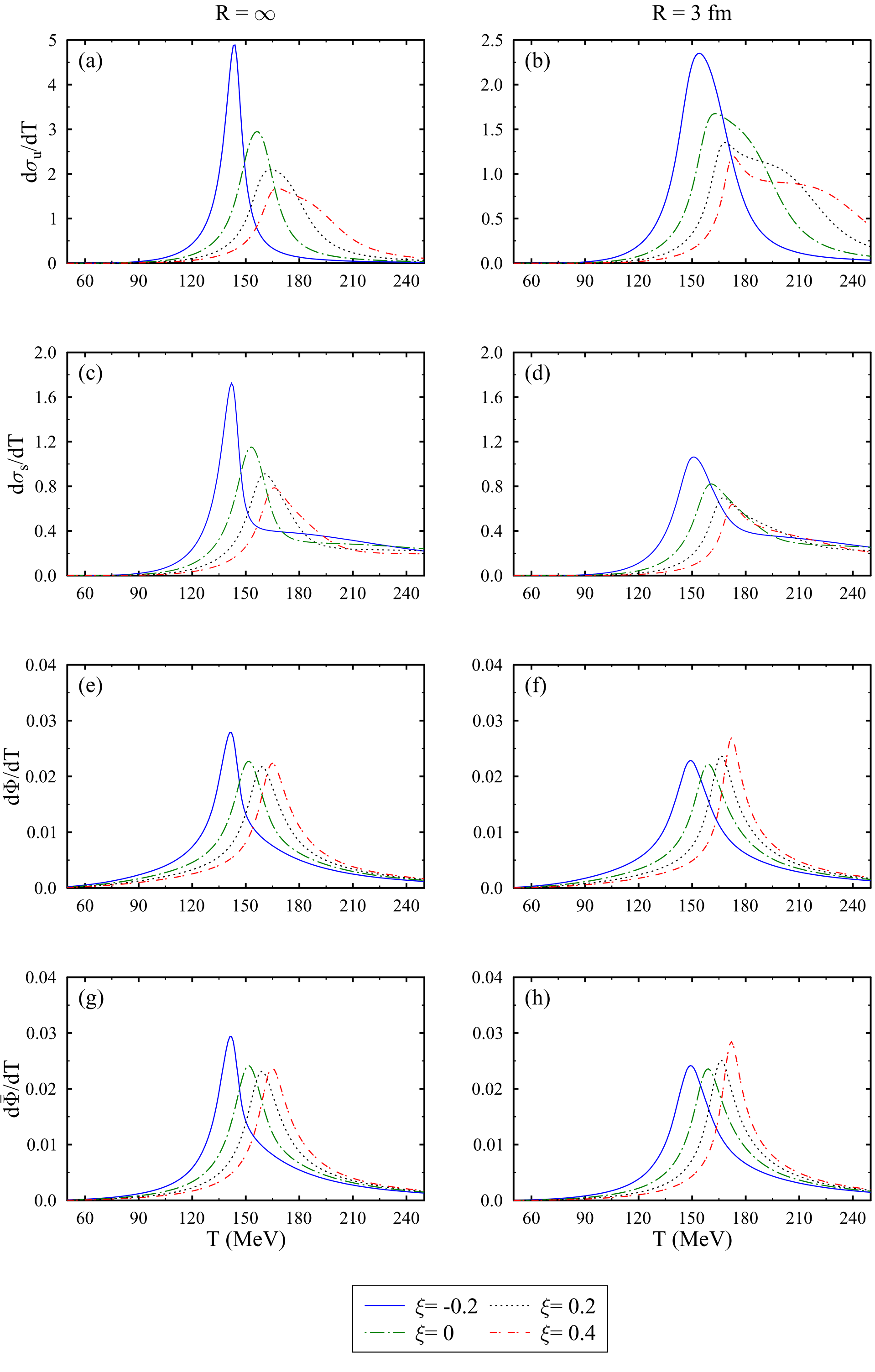

FIG. 11. The derivatives of quark condensates [in subplots (a), (b), (c), and (d)] and Polyakov loop variable [in subplots (e), (f), (g), and (h)] plotted as a function of temperature, T, for anisotropy parameter, $\xi = -0.2$, 0, 0.2 and 0.4. Results are shown for system size $R = \infty$ [in subplots (a), (c), (e), and (g)], and 3 fm [in subplots (b), (d), (f), and (h)] and value of quark chemical potential, μ_q fixed at 0 MeV.

chiral phase boundary and deconfinement transition has been shown in Fig. 12. With the increase of momentum-space anisotropy, the chiral phase boundary shifts to a higher temperature and quark chemical potential values, which was also clear from the behavior of the order parameter. Similarly, the deconfinement boundary also shifts to higher temperature values for increasing ξ. As discussed earlier, the position of the CEP is determined by visualizing

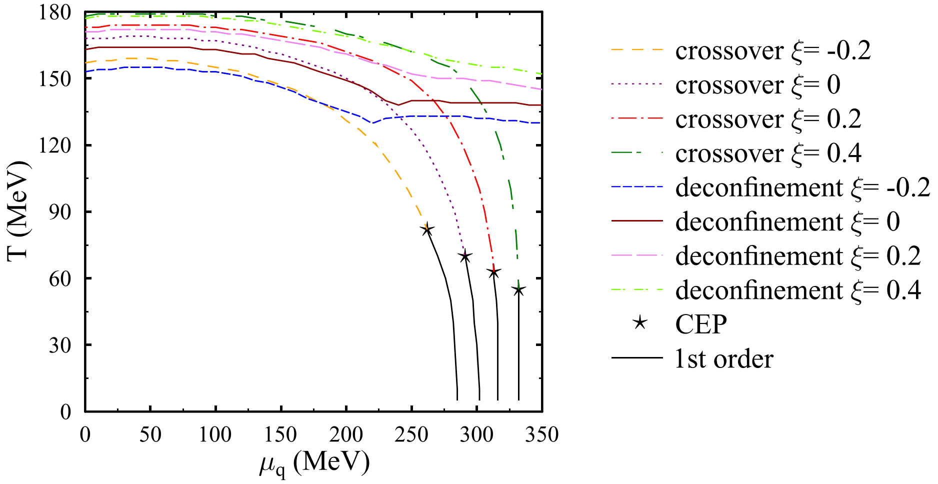

FIG. 12. The QCD phase diagram plotted for varying values of anisotropy parameter, ξ, and vector coupling constant fixed at $g_v = 3.25$.

the derivative of strange and nonstrange quark densities. The CEP for isotropic medium with vector coupling constant $g_v = 3.25$ is $(\mu_{q(CP)}, T_{CP}) = (291, 70)$ MeV. When compared to the value of the critical point for $g_v = 6.5$ in the previous section, the CEP shifts to a higher value of T and low μ_q for decreasing vector coupling [77]. For $\xi = -0.2$, the CEP is observed at $(\mu_{q(CP)}, T_{CP}) = (262, 82)$ MeV, whereas for $\xi = 0.2$, $(\mu_{q(CP)}, T_{CP}) = (313, 63)$ MeV. With further increase in momentum anisotropy parameter to 0.4, $(\mu_{q(CP)}, T_{CP}) = (332, 55)$ MeV. With the change in

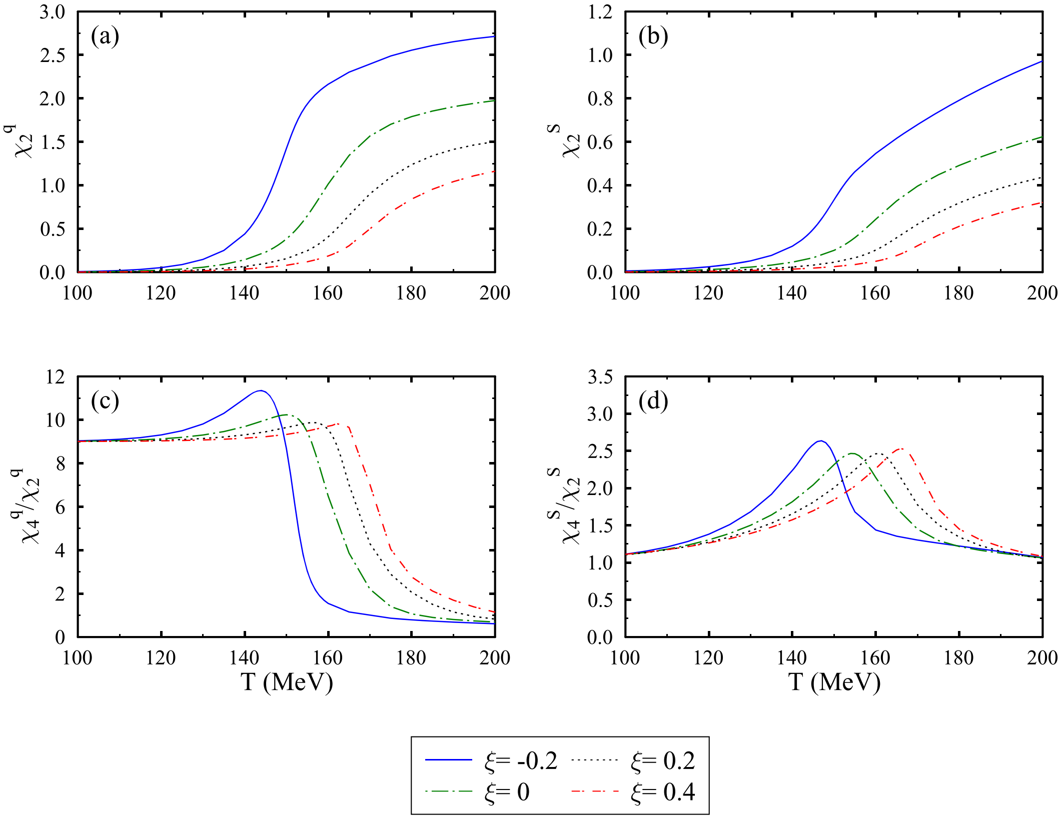

FIG. 13. The second-order susceptibility of quark number, χ_2^q, and kurtosis, χ_4^q/χ_2^q, [in subplots (a) and (c)] and second-order susceptibility of strangeness number, χ_2^S, and kurtosis, χ_4^S/χ_2^S [in subplots (b) and (d)] plotted as a function of temperature, T, for anisotropy parameter, $\xi = -0.2$, 0, 0.2 and 0.4.

the value of ξ from -0.2 to 0.4, there is a rise of 26.7% in $\mu_{q(CP)}$, whereas a fall of 32.9% in the value of $T_{q(CP)}$. In the quark meson model, as the value of ξ changes from -0.4 to 0.4, the CEP has been shown to shift from $(\mu_{q(CP)}, T_{CP}) = (174, 100)$ MeV to $(\mu_{q(CP)}, T_{CP}) = (270, 79)$ MeV [49]. A similar trend in the CEP with increased deviation from the isotropic momentum distribution has been observed in the PNJL model [115]. This shows that with an increase in momentum anisotropy, the first-order phase transition tends to disappear and becomes a crossover.

Figure 13 shows the second-order susceptibility and kurtosis for the quark number in the left column and the strangeness number in the right column for different values of ξ. It is observed that in the phase transition regime, the χ_2^q and kurtosis are stronger for momentum distribution stretched along the direction of anisotropy ($\xi = -0.2$) as compared to the case for isotropic and squeezed momentum distribution ($\xi = 0.2$, 0.4). The value of the critical point at zero value of μ_B for varying ξ changes according to as discussed in Fig. 12. Hydrodynamic simulations and experiments in HICs suggest the existence of a momentum distribution with $\xi > 0$ along the beam direction. It has been shown that in anisotropic quark matter, compared to isotropic conditions, the net baryon kurtosis and skewness values may be heightened, particularly at lower collision energies [115]. This can be investigated in future work by studying the susceptibilities at finite chemical potential.

IV. SUMMARY

To summarize, we have discussed the thermodynamic properties of asymmetric quark matter using the Polyakov quark meson model extended by introducing vector interactions. The effects of strangeness chemical potential, anisotropic momentum distribution, and finite system size have been investigated by analyzing the variation of strange and nonstrange fields at varying temperatures and densities. The derivatives of quark condensates and Polyakov loop variables have been studied to locate the position of the QCD critical point. We have observed that the production of s quarks gets saturated at high-temperature values. The chiral phase boundary for u, d, and s quarks coincides with a crossover transition at lower μ_q before the critical point and a first-order phase transition at higher values of quark chemical potential. The deconfinement phase boundary remains a crossover for all temperature values. With decreasing system volume, the critical point is found to shift to lower values of temperature and higher values of quark chemical potential. On the other hand, the critical point is repositioned to a higher temperature and lower values of quark chemical potential for the decreasing value of strangeness chemical potential. The susceptibilities of conserved charges are enhanced in the transition region. The peak of the kurtosis for the strangeness number gives the value of the critical point to be ≈155 MeV, which is consistent with the lattice QCD studies at zero chemical potential. For increasing the value of the anisotropic momentum parameter, the CEP shifts to lower temperature and higher quark chemical potential values. Thus, investigating the QCD phase diagram in isospin asymmetric quark matter with anisotropic momentum distribution is crucial for enhancing the understanding of phase transitions and critical endpoint. By examining how the phase boundary varies with changing volume, we indicate a heightened possibility of detecting signatures of a CEP in low-energy experiments aiming to produce high baryonic densities, particularly when temperatures are not excessively high. This includes examining the potential fluctuations within the fireball, which can lead to regions with positive and negative net-strangeness and net-isospin, respectively. Understanding the fluctuations of conserved charges through a comparative analysis involving low-energy effective models, lattice QCD, and experimental data is crucial for predicting the phase structure of QCD at high densities [115]. The future experimental programs such as RHIC-BES II data may provide more opportunities to address the uncertainties in understanding the QCD phase structure. In future work, the susceptibilities of conserved charges can be studied at the finite value of chemical potential [116]. The model can be further improvised using the functional renormalization approach [117,118].

ACKNOWLEDGMENTS

The authors sincerely acknowledge the support for this work from the Ministry of Science and Human Resources (MHRD), Government of India, through an Institute fellowship under the National Institute of Technology Jalandhar. A. K. sincerely acknowledges the DST-SERB, Government of India, for funding research project CRG/2019/000096.

---

[1] A. Pandav, D. Mallick, and B. Mohanty, Prog. Part. Nucl. Phys. **125**, 103960 (2022).
[2] A. Ohnishi, Prog. Theor. Phys. Suppl. **193**, 1 (2012).
[3] O. Brüning, H. Burkhardt, and S. Myers, Prog. Part. Nucl. Phys. **67**, 705 (2012).
[4] G. Odyniec, J. Phys. G **37**, 094028 (2010).
[5] L. Kumar and STAR Collaboration, Nucl. Phys. **A904–905**, 256c (2013).
[6] C. Ratti, Rep. Prog. Phys. **81**, 084301 (2018).
[7] C. DeTar and U. Heller, Eur. Phys. J. A **41**, 405 (2009).

[8] H.-W. Lin, Few-Body Syst. **64**, 58 (2023).
[9] R. Gupta, AIP Conf. Proc. **490**, 3 (1999).
[10] J. Liang, T. Draper, K.-F. Liu, A. Rothkopf, Y.-B. Yang (χQCD Collaboration), Phys. Rev. D **101**, 114503 (2020).
[11] M. Petschlies, N. Schlage, A. Sen, and C. Urbach, Eur. Phys. J. A **60**, 9 (2024).
[12] J. N. Guenther, Eur. Phys. J. A **57**, 1 (2021).
[13] S. Muroya, A. Nakamura, C. Nonaka, and T. Takaishi, Prog. Theor. Phys. **110**, 615 (2003).
[14] J. Braun, B. Klein, and B.-J. Schaefer, Phys. Lett. B **713**, 216 (2012).
[15] N. B. Mata Carrizal, E. Valbuena Ordóñez, A. J. Garza Aguirre, F. J. Betancourt Sotomayor, and J. R. Morones Ibarra, Universe **8**, 264 (2022).
[16] H. Georgi, Phys. Lett. B **240**, 447 (1990).
[17] G. Ecker, Prog. Part. Nucl. Phys. **35**, 1 (1995).
[18] D. K. Hong, Phys. Lett. B **473**, 118 (2000).
[19] B. A. Campbell, J. Ellis, and K. A. Olive, Nucl. Phys. **B345**, 57 (1990).
[20] R.-A. Tripolt, J. Braun, B. Klein, and B.-J. Schaefer, Phys. Rev. D **90**, 054012 (2014).
[21] L. Palhares, E. Fraga, and T. Kodama, J. Phys. G **37**, 094031 (2010).
[22] N. Magdy, M. Csanád, and R. A. Lacey, J. Phys. G **44**, 025101 (2017).
[23] N. Magdy, Universe **5**, 94 (2019).
[24] J. Braun, B. Klein, and P. Piasecki, Eur. Phys. J. C **71**, 1576 (2011).
[25] B. Klein, J. Braun, and P. Piasecki, Proc. Sci. LATTICE2011 (**2011**) 199.
[26] P. De Forcrand and O. Philipsen, J. High Energy Phys. 01 (2007) 077.
[27] F. Karsch, C. Allton, S. Ejiri, S. Hands, O. Kaczmarek, E. Laermann, and C. Schmidt, Nucl. Phys. B, Proc. Suppl. **129–130**, 614 (2004).
[28] K. Saha, S. Ghosh, S. Upadhaya, and S. Maity, Phys. Rev. D **97**, 116020 (2018).
[29] L. Abreu and E. Nery, Int. J. Mod. Phys. A **31**, 1650128 (2016).
[30] L. Abreu, A. Malbouisson, and J. Malbouisson, Phys. Rev. D **84**, 065036 (2011).
[31] L. Abreu, E. Nery, and A. Malbouisson, Phys. Rev. D **91**, 087701 (2015).
[32] L. Abreu, A. Malbouisson, and J. Malbouisson, Europhys. Lett. **90**, 11001 (2010).
[33] S. Pal, A. Motornenko, V. Vovchenko, A. Bhattacharyya, J. Steinheimer, and H. Stoecker, Phys. Rev. D **109**, 014009 (2024).
[34] N. Chahal, S. Dutt, and A. Kumar, Phys. Rev. C **107**, 045203 (2023).
[35] A. Bhattacharyya, P. Deb, S. K. Ghosh, R. Ray, and S. Sur, Phys. Rev. D **87**, 054009 (2013).
[36] L. Abreu, M. Gomes, and A. da Silva, Phys. Lett. B **642**, 551 (2006).
[37] A. Bhattacharyya, R. Ray, and S. Sur, Phys. Rev. D **91**, 051501 (2015).
[38] B. S. Kasmaei, M. Nopoush, and M. Strickland, Phys. Rev. D **94**, 125001 (2016).
[39] S. Mrówczyński, B. Schenke, and M. Strickland, Phys. Rep. **682**, 1 (2017).
[40] P. Romatschke and M. Strickland, Phys. Rev. D **68**, 036004 (2003).
[41] D. Bödeker and K. Rummukainen, J. High Energy Phys. 07 (2007) 022.
[42] M. E. Carrington, B. M. Forster, and S. Makar, Phys. Rev. C **104**, 064908 (2021).
[43] B. S. Kasmaei and M. Strickland, Phys. Rev. D **97**, 054022 (2018).
[44] L. Bhattacharya, R. Ryblewski, and M. Strickland, Phys. Rev. D **93**, 065005 (2016).
[45] B. Schenke and M. Strickland, Phys. Rev. D **76**, 025023 (2007).
[46] B. S. Kasmaei and M. Strickland, Phys. Rev. D **99**, 034015 (2019).
[47] L. Thakur, P. Srivastava, G. P. Kadam, M. George, and H. Mishra, Phys. Rev. D **95**, 096009 (2017).
[48] P. Srivastava, L. Thakur, and B. K. Patra, Phys. Rev. C **91**, 044903 (2015).
[49] H.-X. Zhang and B.-W. Zhang, Chin. Phys. C **45**, 044104 (2021).
[50] P. Braun-Munzinger, J. Stachel, J. Wessels, and N. Xu, Phys. Lett. B **344**, 43 (1995).
[51] P. Braun-Munzinger, I. Heppe, and J. Stachel, Phys. Lett. B **465**, 15 (1999).
[52] P. Kovács and Z. Szép, Phys. Rev. D **77**, 065016 (2008).
[53] J. Rafelski, Eur. Phys. J. Spec. Top. **155**, 139 (2008).
[54] P. Koch, B. Müller, and J. Rafelski, Int. J. Mod. Phys. A **32**, 1730024 (2017).
[55] P. Bhagat and A. Bhasin, Few-Body Syst. **64**, 69 (2023).
[56] G. Bendiscioli, T. Bressani, L. Lavezzi, A. Panzarasa, and P. Salvini, Nucl. Phys. **A815**, 67 (2009).
[57] V. Dexheimer, R. Negreiros, and S. Schramm, Phys. Rev. C **91**, 055808 (2015).
[58] D. Toublan and J. B. Kogut, Phys. Lett. B **605**, 129 (2005).
[59] A. Mukherjee, A. Bhattacharyya, and S. Schramm, Phys. Lett. B **797**, 134899 (2019).
[60] W. Fan, X. Luo, and H. Zong, Chin. Phys. C **43**, 033103 (2019).
[61] S. Chatterjee and K. A. Mohan, Phys. Rev. D **86**, 114021 (2012).
[62] S. Borsanyi, Z. Fodor, S. D. Katz, S. Krieg, C. Ratti, and K. Szabo, J. High Energy Phys. 01 (2012) 138.
[63] M. Arslandok *et al.* (ALICE Collaboration), Nucl. Phys. **A1005**, 121979 (2021).
[64] S. Pal, G. Kadam, H. Mishra, and A. Bhattacharyya, Phys. Rev. D **103**, 054015 (2021).
[65] A. Bhattacharyya, R. Ray, and S. Sur, DAE Symposium on Nuclear Physics **59**, 708 (2014).
[66] T. Beisitzer, R. Stiele, and J. Schaffner-Bielich, Phys. Rev. D **90**, 085001 (2014).
[67] A. Zacchi, R. Stiele, and J. Schaffner-Bielich, Phys. Rev. D **92**, 045022 (2015).
[68] L. Ferroni and V. Koch, Phys. Rev. C **83**, 045205 (2011).
[69] R. C. Pereira, R. Stiele, and P. Costa, Eur. Phys. J. C **80**, 712 (2020).
[70] N. Chahal, S. Dutt, and A. Kumar, Chin. Phys. C **46**, 063104 (2022).
[71] A. Zacchi, M. Hanauske, and J. Schaffner-Bielich, Phys. Rev. D **93**, 065011 (2016).

[72] B. W. Mintz, R. Stiele, R. O. Ramos, and J. Schaffner-Bielich, Phys. Rev. D **87**, 036004 (2013).

[73] V. Skokov, B. Stokić, B. Friman, and K. Redlich, Phys. Rev. C **82**, 015206 (2010).

[74] K. Otto, M. Oertel, and B.-J. Schaefer, Phys. Rev. D **101**, 103021 (2020).

[75] P. Kovács, Z. Szép, and G. Wolf, Phys. Rev. D **93**, 114014 (2016).

[76] G. t Hooft, Phys. Rev. Lett. **37**, 8 (1976).

[77] H. Ueda, T. Z. Nakano, A. Ohnishi, M. Ruggieri, and K. Sumiyoshi, Phys. Rev. D **88**, 074006 (2013).

[78] T. K. Herbst, Ph.D. thesis, Graz, 2012.

[79] K. Fukushima and V. Skokov, Prog. Part. Nucl. Phys. **96**, 154 (2017).

[80] A. M. Polyakov, Phys. Lett. B **72**, 477 (1978).

[81] C. Borgs and E. Seiler, Commun. Math. Phys. **91**, 329 (1983).

[82] A. G. Grunfeld and G. Lugones, Eur. Phys. J. C **78**, 640 (2018).

[83] C. Ratti, M. A. Thaler, and W. Weise, Phys. Rev. D **73**, 014019 (2006).

[84] R. Stiele, E. S. Fraga, and J. Schaffner-Bielich, Phys. Lett. B **729**, 72 (2014).

[85] C. Vafa and E. Witten, Nucl. Phys. **B234**, 173 (1984).

[86] J. T. Lenaghan, D. H. Rischke, and J. Schaffner-Bielich, Phys. Rev. D **62**, 085008 (2000).

[87] U. S. Gupta and V. K. Tiwari, Phys. Rev. D **85**, 014010 (2012).

[88] S. Chatterjee and K. A. Mohan, Phys. Rev. D **85**, 074018 (2012).

[89] M. Kitazawa, T. Koide, T. Kunihiro, and Y. Nemoto, Nucl. Phys. **A721**, C289 (2003).

[90] A. Bhattacharyya, R. Ray, S. Samanta, and S. Sur, Phys. Rev. C **91**, 041901 (2015).

[91] L. M. Abreu, A. P. Malbouisson, and J. M. C. Malbouisson, Phys. Rev. D **83**, 025001 (2011).

[92] F. C. Khanna, *Thermal Quantum Field Theory: Algebraic Aspects and Applications* (World Scientific, Singapore, 2009).

[93] J. Schwinger, Phys. Rev. **82**, 914 (1951).

[94] J. I. Kapusta and K. A. Olive, Nucl. Phys. **A408**, 478 (1983).

[95] B. Klein, Phys. Rep. **707–708**, 1 (2017).

[96] L. M. Abreu, E. S. Nery, and E. B. Corrêa, Physica (Amsterdam) **572A**, 125885 (2021).

[97] E. Ferrer, V. Gusynin, and V. de La Incera, Phys. Lett. B **455**, 217 (1999).

[98] K. Redlich and K. Zalewski, arXiv:1611.03746.

[99] S. Carignano, M. Buballa, and W. Elkamhawy, Phys. Rev. D **94**, 034023 (2016).

[100] G. Torrieri, J. Phys. G **32**, S195 (2006).

[101] C. Greiner, D.-H. Rischke, H. Stoecker, and P. Koch, Phys. Rev. D **38**, 2797 (1988).

[102] A. D. Panagiotou and P. G. Katsas, arXiv:hep-ph/0204011.

[103] J. Letessier, A. Tounsi, U. W. Heinz, J. Sollfrank, and J. Rafelski, Phys. Rev. D **51**, 3408 (1995).

[104] J. B. Kogut and D. K. Sinclair, Phys. Rev. D **70**, 094501 (2004).

[105] A. Ohnishi, H. Ueda, T. Nakano, M. Ruggieri, and K. Sumiyoshi, Phys. Lett. B **704**, 284 (2011).

[106] G. Kovács, P. Kovács, G. Wolf, P. M. Lo, and K. Redlich, Phys. Rev. D **108**, 076010 (2023).

[107] L. M. Abreu, E. B. Corrêa, C. A. Linhares, and A. P. Malbouisson, Phys. Rev. D **99**, 076001 (2019).

[108] M. Stephanov, Prog. Theor. Phys. Suppl. **153**, 139 (2004).

[109] N. Antoniou, Proc. Sci. CORFU2016 (**2017**) 052.

[110] Y. Aoki, G. Endrődi, Z. Fodor, S. D. Katz, and K. K. Szabó, Nature (London) **443**, 675 (2006).

[111] H. Mao, J. Jin, and M. Huang, J. Phys. G **37**, 035001 (2010).

[112] M. Kumari and A. Kumar, Eur. Phys. J. Plus **136**, 19 (2021).

[113] H.-T. Ding, Nucl. Phys. **A931**, 52 (2014).

[114] M. Asakawa, S. A. Bass, and B. Müller, Prog. Theor. Phys. **116**, 725 (2006).

[115] W.-b. He and G.-y. Shao, Phys. Rev. D **108**, 114012 (2023).

[116] W. Fan, X. Luo, and H. Zong, Chin. Phys. C **43**, 054109 (2019).

[117] N. Dupuis, L. Canet, A. Eichhorn, W. Metzner, J. M. Pawlowski, M. Tissier, and N. Wschebor, Phys. Rep. **910**, 1 (2021).

[118] W.-j. Fu, Commun. Theor. Phys. **74**, 097304 (2022).